

AFOSR-TR- 94 0161

Approved for public release;
distribution unlimited.

TABLE OF CONTENTS

<u>Section</u>	<u>Page No.</u>
Abstract	1
1.0 INTRODUCTION	2
2.0 DESIGN, DEVELOPMENT AND CALIBRATION OF THE LENS FACILITY	4
3.0 MODELS FOR AEROTHERMAL AND AERO-OPTICAL INSTRUMENTATION EVALUATION STUDIES	6
3.1 Model Support and Optical Bench System	6
3.2 Models for Seeker-Head Validation Studies	6
3.2.1 Flat Plate Models	7
3.2.2 2-D Wedge Model	7
3.2.3 3-D Triconic Validation Model	8
3.3 Surface and Flowfield Instrumentation	8
3.3.1 Surface Instrumentation	9
3.3.2 Flowfield Instrumentation	9
3.4 Aero-optic Instrumentation	10
3.4.1 Introduction	10
3.4.2 Refractive Instruments	11
4.0 VALIDATION AND EVALUATION STUDIES WITH THE 2-D MODEL CONFIGURATIONS	17
4.1 Introduction	17
4.2 Objectives and Design of the Experimental Studies	17
4.3 Aerothermal Measurements on 2-D Seeker-Head Configurations	18
4.4 AO Measurements	19
4.4.1 Validation of Interferometry Analysis	19
4.4.2 Data Analysis	23
5.0 SUMMARY AND CONCLUSIONS	26
References	27
Figures	28

94-12125



94 4 20 054

Abstract

This report describes recent developments in the LENS facility, flow field calibration studies, and aerothermal and aero-optical measurements to evaluate the turbulent flow field characteristics of seeker head configurations in hypervelocity airflow. The development of the LENS facility to run at pressure levels up to 30,000 psi and temperatures up to 14,000°R are reviewed. Issues associated with diaphragm performance, reservoir configuration, throat melting and burning, and modifications to the facility for large recoil loads at high pressure operation are briefly reviewed. Flow field measurements made during calibration studies are compared with computer predictions. Validation studies with simple seeker head aperture configurations in high enthalpy flows are then discussed. The models and aerothermal and aero-optical instrumentation used in these studies are described. The measurements obtained in flows up to 12,000 ft/sec are compared with similar measurements at lower velocities, simple correlation techniques, and detailed computer simulations.

Accession For	
NTIS GRA&I	<input checked="" type="checkbox"/>
DTIG TAB	<input type="checkbox"/>
Unannounced	<input type="checkbox"/>
Justification	
By	
Distribution/	
Availability Notes	
Dist	Avail and/or Special
A-1	

1.0 INTRODUCTION

During the past year, the Large Energy National Shock (LENS) tunnel has been completed, and development and calibration studies conducted examine seeker-head characteristics. This facility has been used to examine the flow field characteristics over simple seeker head aperture configurations in high Reynolds number flow fields for velocities up to 12,000 ft/sec. The availability of this ground based facility, which can duplicate the flow field environment around full-scale hypervelocity endoatmospheric seeker heads, provides a key element in the development and evaluation of hypervelocity interceptors prior to flight testing. Both the aerothermal and aero-optic characteristics of such a configuration can be examined simultaneously to evaluate the potential survival of the configuration and the image obscuration and degradation resulting from flow field radiation and shock layer density gradients. To duplicate this harsh environment, a ground test facility must be capable of generating sufficiently large Reynolds numbers to replicate the transitional and turbulent nature of the boundary layer over the vehicle, and duplicate the interceptor velocity thereby generating the exact radiation characteristics developed in the shock layer as well as the mixing characteristics of the coolant layer over the window. Thus, the key freestream parameters which must be generated in a ground test facility are Reynolds number and total temperature. The performance of the LENS facility in generating such characteristics is compared with other ground test facilities for hypervelocity interceptor trajectories in Figure 1. The LENS facility can be used to generate the typical fly-out and homing characteristics of the hypervelocity endo interceptor, whereas other more conventional ground test facilities are not capable of generating the high enthalpies and high Reynolds number conditions necessary to duplicate the homing environment. In addition to the development of a facility to generate the correct total temperature and pressure levels, a suite of aerothermal and aero-optic instrumentation must be developed to accurately characterize the local environment around the vehicle and the heating and image distortions characteristic of a specific aperture configuration. Because of the severity of this environment and the large loads generated during the operation of such a facility, the development of the instrumentation represents a key part of the assembly of such an evaluation facility. Figure 2 shows the current performance of the LENS facility to duplicate the environment around many of the current hypersonic interceptor designs. Because of the high Reynolds number capabilities of the LENS facility, as shown in Figure 3, it is also suitable for the aerothermodynamic testing of air breathing hypersonic cruise vehicles and accelerators.

During the past year, we have been conducting development studies in the LENS facility to bring the facility and the instrumentation suite to the point where seeker head evaluation studies can be conducted under conditions close to maximum operating conditions. In this report, we briefly review the developments in the performance of the LENS facility in the areas of diaphragm performance, recoil load control, reservoir region thermal protection, and throat melting and burning. We also discuss the addition of a high volume compressor system and dump tank assembly to the initial LENS configuration. The instrumentation and calibration of the facility is reviewed. The models and aerothermal and aero-optic instrumentation which are being assembled and used in the facility validation and seeker head evaluation studies are then described. We then describe measurements made using simple 2-dimensional seeker-head configurations to evaluate flow quality and performance of the aero-optic instrumentation as well as the aerothermal and aero-optical characteristics of the flow over seeker-head configurations at velocities up to 12,000 ft/sec. These studies include the evaluation of the relative effectiveness of nitrogen and helium coolants. Measurements made in these studies are compared with those made in earlier studies at lower velocities, simple correlation techniques, and predictions based on Navier-Stokes calculations.

2.0 DESIGN, DEVELOPMENT AND CALIBRATION OF THE LENS FACILITY

The LENS facility is a large, reflected shock tunnel that was constructed to study turbulent mixing and real gas effects over hypervelocity vehicles. The design of the facility was based on shock tunnels developed earlier at Calspan and incorporates a number of features that have evolved over the past 25 years of shock tunnel development, as well as some new design features. LENS is a chambered shock tunnel having a 24-foot long driver tube with an internal diameter of 12 inches and a driven tube of 8-inches in diameter, which is 60 feet long. The basic layout of the LENS facility is shown in Figure 4. The driver section of the tunnel is heated to 750°F, and because of hydrogen operation, is fitted with a stainless steel liner to prevent hydrogen embrittlement. The driver section of the tunnel (shown in Figure 5) can be operated at pressures up to 30,000 psi, and because of its large volume, a new high pressure, high flow rate compressor (shown in Figure 7) was installed to provide a pumping capacity which will fill the driver in approximately one hour. The driver and heater section of the tunnel are mounted on carriages which recoil with the tunnel as it is fired. A double diaphragm rig is used to initiate the flow in tunnel. Here, two diaphragms are separated by an intermediate chamber which is held at approximately half the driver pressure; the pressure in the intermediate chamber is rapidly increased to fire the tunnel. Diaphragms of over 18 inches in diameter and 1.25 inches thick are employed to obtain controlled bursts with the minimum amount of fragmentation. One such diaphragm is shown in Figure 6, and because of its large weight, two people are required to lift it into position. Because flow field chemistry and cleanliness are of prime importance in this facility, all components that come in contact with the test gas are constructed from stainless steel. Components of the stainless steel driven tube, shown in Figure 8, are fastened together with high strength tensile bolts which are prestressed so that despite the 2-4 million pound recoil loads, there are no gaps generated between driven tube components. A centerbody apparatus, which employs a fast-acting plug valve to close the nozzle throat, is used to terminate the flow once the uncontaminated volume of shock-heated air has been exhausted from the reservoir region of the shock tube. The reservoir and centerbody region of the shock tunnel is lined with copper in order to prevent burning. Copper, molybdenum and tungsten can be used for the throat section of the tunnel to prevent melting and burning. Because the high heating rates generating in the nozzle are concentrated in a relatively small region close to the throat, the major portion of the contoured nozzle can be constructed from fiberglass. To handle the large loads generated by the recoil of the tunnel, a metal corset, which surrounds the fiberglass nozzle, is used to couple the driven tube with the test section. Shown in Figure 8, is the Mach 11 to 18

contoured fiberglass nozzle, which has an exit plane diameter of 48 inches. Mach 6 and 8 nozzles will subsequently be available. The test section, shown in Figure 9, has an internal diameter of 96 inches, and has been constructed so that it can be coupled to nozzles with exit planes of up to 72 inches in diameter. Because of the large volume of gas contained in the high-pressure driver, a large test-section volume is required to prevent the test section pressure from reaching levels that would fracture the schlieren windows. Under normal operation, when the centerbody valve closes, the basic test-section volume is sufficient to prevent overpressurization. However, if the centerbody fails to close, an additional volume is provided by a ballast tank. This ballast tank is coupled to the test section through a large diameter pipe with a mylar diaphragm separating the test section from the ballast tank. The control room of the shock tunnel, which is shown in Figure 10, employs similar control systems and instrumentation layouts as employed in the earlier shock tunnels at Calspan. Because of the specific operation of the shock tunnel, we chose not to automate its running with a computer monitor controlled system.

The large size of the LENS driver and driven tubes provides the capabilities to obtain test times of up to 18 milliseconds at velocities of 5,000 ft/sec and 3-4 milliseconds of uncontaminated test time at 16,000 ft/sec. The velocity/altitude performance of the LENS facility is shown in Figure 11, with annotations giving the points at which the tunnel is calibrated for helium operation. Also shown are the ENDO LEAP test points. Currently, we are exploring the possibility of running in a nonreflective mode for high enthalpy airflows and adding a buffer section of the tunnel to enable us to obtain velocities in excess of 20,000 ft/sec. In Figure 12, the Mach number, Reynolds number capabilities of the LENS facility are compared with the performance of other high Reynolds number facilities. Figures 13 and 14 show typical temperature and Mach number calibrations of the D-nozzle employed in the LENS facility. We employ total temperature, pitot pressure, and cone probes to calibrate low enthalpy flows and add electron beam and absorption techniques to obtain freestream properties and concentration levels in the high enthalpy flows.

3.0 MODELS FOR AEROTHERMAL AND AERO-OPTICAL INSTRUMENTATION EVALUATION STUDIES

3.1 Model Support and Optical Bench System

The model support and optical bench system is one of the most important components of the aero-optic evaluation system. The specification that the optical bench system does not sustain more than a 10 microradian distortion during the run time of the tunnel, places a stringent requirement on the design of this system. As discussed earlier, the basic components of the shock tunnel; the driver, driven tube, and test section are mounted on rollers and are free to move during the tunnel operation. However, the basic sting system is not attached to these components and, thus, is not subjected to the large acceleration loads associated with the tunnel recoil. As shown in Figure 15, the lower half of the support system is attached to the concrete floor beneath the test section through two massive rods that pass through the test section via four sets of rolling seals. The massive (40,000-lb) upper half of the support system is supported on four rubber blocks giving this system has a natural frequency of under 20 hertz which will totally isolate the model from recoil loads during the 4- to 18-millisecond test time of the tunnel. To prevent the model support structure from being exposed to the airflow, it is surrounded by fairings which are attached directly to the test section of the tunnel. The optical bench system, is suspended inside the model support system. The optical bench is supported atop vibration isolated mounts, which on a massive concrete block which is in turn isolated from the tunnel floor. The entire system is constructed so that the components on the optical bench are at atmospheric pressure and temperature. This allows conventional instrumentation and the venting of sensor coolant gases which might be employed on some seeker-head configurations.

3.2 Models for Seeker-Head Validation Studies

There are three models that are being used to validate the performance of the tunnel and aero-optic instrumentation, and obtain fundamental information on the aerothermal and aero-optical characteristics of the shock layer and turbulent boundary layer flows over typical seeker-head configurations. The first of these models is a flat plate configuration designed to provide data on the aero-optical quality of the freestream and the flow over the forebody. The second configuration is basically a two-dimensional representation of a seeker-head configuration designed to provide easily interpretable experimental data and a

flow field configuration that can be computed easily to minimize the assumptions involved in the modeling of turbulence and the intrinsic three-dimensional effects which are associated with typical three-dimensional seeker-head configurations. A triconic nosetip will be employed to provide a configuration very similar to those of current seeker-head designs so that the refractive, imagery, and radiative instrumentation suite can be developed before it is used to evaluate the relative merits of competitive designs.

3.2.1 Flat Plate Models

The flat plate model used in our initial studies is shown in Figure 16. This model was designed to replicate the flow field over the forebody from which the beam is transmitted into the seeker-head window. We employ a small leading edge bluntness to stabilize the boundary layer over the forebody and the flat plate, which coupled with the short length of boundary layer before the window, should insure that the boundary layer over both the flat plate and the forebody window remains laminar under most flow conditions.

3.2.2 2-D Wedge Model

The wedge model (shown in Figure 17) represents a 2-D equivalent of an axisymmetric seeker-head configuration. In the design of this configuration, we have incorporated a number of features which may be required on an equivalent 3-D configuration to control the heating levels to the forebody and the window. Thus, the nosetip and frustra upstream of the window are independently transpiration cooled, and the seeker-head window is film-cooled in a manner similar to those that have been and could be employed on a typical 3-D seeker-head configuration. The transpiration-cooled segment of the model is designed so that the coolant is injected into the flow in a subsonic stream from a large number of small holes in the model surface, each of which are controlled from seven tiny sonic orifices at their base. In this way, we can control the flow rate through the model independently from the pressure on the surface of the model. The injector system, which controls the film cooling, was designed for a nitrogen coolant issuing at Mach 2 from the exit plane of the 2-dimensional nozzle configuration. The slot height was designed from calculations employing the HEDI correlation to obtain a fully cooled window under matched conditions at test point 3. Figure 18 shows the injection system and the contour of the 2-dimensional nozzle. The transpiration surfaces in the nosetip and forebody were designed to obtain flow rates which were 10 and 2 percent, respectively of

the freestream mass flow rate in the freestream. The reservoirs which supply the flows through the nosetip, wedge, and injector system are connected through six valcor valves (one each for nose and wedge and four for the coolant slot) to reservoirs mounted at the base of the model support system. The flows through the model are initiated so that equilibrium is obtained just prior to flow initiation through the tunnel. The pressures throughout this system are monitored to obtain accurate measurements of flow rate. The 2-D wedge is instrumented with pressure and calorimeter and thin-film heat transfer instrumentation. The model was designed so that either an optical window or an insert containing pressure and heat transfer instrumentation can be inserted into the window section.

3.2.3 3-D Triconic Validation Model

The 3-D triconic mode shown in Figure 19, is representative in configuration and size of the small seeker heads being currently considered for ENDO-interceptor applications. The triconic configuration enables a window to be placed in a flat section through the three conic surfaces, as shown in Figure 20. An injector system, similar in principal to that employed in the 2-D model, is used to cool this surface in which the window is inset. In this 3-D configuration, the nosetip segment of the model is interchangeable so that either internally-cooled or transpiration-cooled configuration can be employed. We will employ a backfaced cooled configuration in our studies. The injector configuration (shown in Figure 20) and the size of the film-cooling system was determined from the low velocity HEDI correlation for ENDO LEAP test condition 3. As shown in Figure 19, this triconic configuration is extensively instrumented with heat transfer and pressure gages. Again, a instrumented insert is used to replace the optical window for aerothermal measurements.

3.3 Surface and Flowfield Instrumentation

A suite of intrusive and nonintrusive aerothermal instrumentation is being assembled for aerothermal testing in the LENS facility. Table 1 shows a summary of surface and flow field instrumentation which has been developed and used in the shock tunnels over the past 30 years. There are two categories of instrumentation shown under flow field instrumentation, these are intrusive or probe instrumentation and nonintrusive beams which are propagated through the flow from the model or tunnel walls and observed with remote sensors.

3.3.1 Surface Instrumentation

Thin-film, calorimeter, and coaxial heat transfer instrumentation are routinely used to obtain heat transfer measurements in the shock tunnel, Ref. 2. Of these, the thin-film technique is the most well-developed and capable of time-resolved measurements up to 1 MHz. However, thin-film instrumentation can be abraded in high enthalpy flows, and under such conditions, calorimeter and coaxial instrumentation provide alternative methods for measuring heat transfer rate. Figure 21 shows a typical installation of a 1/8-inch diameter thin-film and calorimeter instrumentation (Figure 22) into the instrumented window section for the 2-D wedge model. We have extensively used PCB and Kulite pressure transducers to obtain pressure measurements on models and basic tunnel components. The piezoelectric PCB transducer is generally employed beneath an orifice whereas the Kulite strain gage transducer is generally flush mounted. In both cases, precautions are taken to prevent large heating loads from influencing the output of the transducer. Skin-friction measurements have been obtained with single component force balances which are both acceleration and normal pressure compensated. This miniaturized force balance in which the sensing element is mounted flush with the surface can be constructed with diameters as small as 3/8 of an inch see Figure 23. A specialized form of heat transfer gage to measure gas cap radiation is one in which thin-film instrumentation is mounted on the front and back surfaces of a transparent quartz element. Gas cap radiation can be determined from the output of the two thin-film sensors. Flush mounted electrostatic probes have been routinely used to obtain measurements which can be related to the electron density in highly ionized nonequilibrium airflows.

3.3.2 Flowfield Instrumentation

Intrusive Instrumentation—Three sets of instrumentation are used to probe the flow field under low-enthalpy conditions. These are mean-frequency pitot probes, total temperature probes, and thin-film probes. A typical probe assembly is shown in Figure 24. The Kulite-based high-frequency pitot probes have a frequency response of 300 KHz. The total temperature gages (a shielded platinum rhodium thermocouple probe) and the thin-film gages will give us the ability to measure fluctuations of up to 1 KHz and 500 KHz, respectively. Both the pitot pressure and thin-film instruments can be used to obtain turbulent scale size in the mixing region of the flow field. In flows with mixtures of nonreacting gases, gas sampler probes have been used to obtain the relative concentrations of the constituents. Such a probe is basically a pitot tube with a shutter chamber at its base.

During the test time, the shutter is opened to allow a gas sample into the chamber. The shutter is closed before the end of the test duration and the sample thus collected is subsequently analyzed with gas chromatography. Ion or langmuir probes have been used extensively to obtain measurements of electron density in ionized nonequilibrium airflows around blunt bodies. This technique which employs fine tungsten wires supported in a pyrex base, has been shown to be a relatively simple and successful high resolution technique. Total enthalpy probes, which are based on analyzing the heat transfer rate to simple configurations or determining the energy content of the flow, have been used in shock tunnel studies.

Non-intrusive Instrumentation—We will be using a number of non-intrusive flow field measurement techniques during the experimental studies. We use schlieren photography and holographic interferometry to determine the distribution of the density in the flow field over the models. This will enable us to determine the boresight shift for direct comparisons with the boresight-shift data obtained from line-of-sight measurement through the window. Electron beam techniques have been used in earlier shock tunnel studies (Reference 2) to obtain mean and fluctuating density measurements across turbulent boundary layers in hypersonic flow. Static temperature measurements can also be obtained at the same point that the density measurements are made. Laser induced fluorescence (LIF) has been used successfully in shock tunnel studies to measure flow field properties and species concentrations. This technique is currently being developed for the LENS facility. Absorption spectroscopy has been used during the calibration phase of the LENS facility to examine species concentration, and microwave interferometry instrumentation is available in a form previously used to examine plasmas over re-entry nose shapes.

3.4 Aero-optic Instrumentation

3.4.1 Introduction

The refractive and radiative environment generated over the window must be determined to evaluate the optical performance of the seeker head. Non-uniform and turbulent flows over the window introduce refractive effects that degrade the optical performance of the sensor looking through the flow. The optical wavefront distortion blurs, shifts and jitters the target image on the focal plane of the sensor, thus degrading line-of-sight data sent to the guidance and control system. Also, radiative emissions from high-temperature air coolants reach the sensor, raising background levels and degrading

performance. The optical evaluation of the sensor in the LENS facility is based on direct measurements of refractive and radiative levels produced in the flow. The radiative environment achieved in the high-temperature flow over the seeker head produces an increased background level on the focal plane and absorbs incident target radiation. These radiation levels are expected to depend on incident-gas velocity and density, coolant gas and seeker-head design.

The AOEC instrumentation suite, Figure 25, utilizes visible and infrared (IR) light sources, a wide -band optical bus and refractive and radiative sensors. The light sources are a 6-pulse ruby laser system, a HeNe laser and a blackbody source. The light is combined into a wide-band collimated beam (50mm diameter) and directed into the LENS facility. The optical bus in the test section directs the beam through a window, into the flow and into the seeker head aperture. The return arm of the optical bus directs the beam from the seeker head to the sensor suite.

For the refractive sensors, the IR band is split from the visible bands. An image is formed with the IR light on a two-dimensional focal plane array (FPA) sensor. The visible light is split between three sensors; holography, imager and boresight. The ruby laser beam is directed at the hologram where it is mixed with the reference beam. The HeNe laser beam is split between the two-dimensional FPA imaging sensor and the quadrant detectors which measure boresight deflections. The refractive sensors all operate simultaneously during the shock tunnel flow.

For the radiative sensors, the light sources are not used, except for the blackbody in calibration. The radiative sensors measure mid-wave infrared (MWIR) emission in the presence of shock tunnel flow. The radiation emitted from the flow is collected in the optical bus and relayed to the radiometer and the spectrometer. The radiometer can be configured with one of eight spectral filters in the MWIR. The spectrometer resolves the 1.5 to 5.0 micron band onto a 32 pixel linear array. The two radiative instruments operate simultaneously during the shock tunnel flow. The refractive and radiative sensors do not operate simultaneously, as the radiative sensor obscures the refractive sensor.

3.4.2 Refractive Instruments

The refractive degradation's are measured with a combination of wavefront-distortion and image-formation diagnostics. The wavefront distortion produced by the

flow over the seeker head can be measured directly with holographic interferometry. Pulsed-laser holography is a practical and accurate means for interferometric measurements of wavefront distortion. With attendant specification of the seeker aperture and wavelength, the focal-plane intensity distribution can be obtained through Fourier analysis. The holographic-interferometry diagnostic provides direct wavefront distortion measurements. The analysis, provides image blur, modulation transfer function and point spread function data for the wavelength and aperture size of interest that are in the ultraviolet, visible or IR band. The alternative to wavefront measurement in the input aperture is to measure intensity in the focal plane. This is accomplished by focusing the beam onto a camera. This direct image-formation approach has the advantage of producing a real image (i.e., with actual lens elements) and recording real intensity distributions. This bypasses the analysis-intensive step used in holographic interferometry of high resolution phase measurements and two-dimensional Fourier transformation. The distinct disadvantage of the direct image-formation approach is that the optical degradation is wavelength and aperture dependent; therefore, this evaluation is less comprehensive than the holographic interferometry diagnostic. The boresight sensor measures the time resolved line-of-sight deflections. The imagery diagnostic provides direct measurement of boresight error, jitter and image blur, in the visible and IR bands.

Holographic Interferometry

Aero-optic holographic interferometry provides visual and quantitative measurements of the optical effects of coolant turbulence. Direct measurements of optical-wavefront distortion are achieved through interference with a plane optical wave. Holographic interferometry is accomplished by recording both the plane (flow-off) and the distorted (flow-on) wavefronts. When reconstructed, such holograms reproduce both wavefronts, and the resulting interference depicts the flow-on wavefront distortion. The two waves are superimposed with the incorporation of a double-plate hologram reconstruction device. In reconstruction, the holograms are selected to achieve either the infinite or finite fringe configuration. The interference fringes depict the changes produced by the flow. This approach is known as single-pulse holographic interferometry, since only one flow-on exposure is used.

The holographic interferometer, Figure 26, uses a pair of triple-pulse ruby lasers, each used to record three holograms at a nominal spacing of 100 microseconds. The pair of laser beams are combined and directed into the optical bus. Within the optical bus, the

beams are directed into the flow field and the seeker head apertures, and finally returned to the sensor platform. The beams from each laser are separated and directed at individual holograms, that is, each laser exposes three holograms on its individual plate. The reference beams are multiplexed in angle by 5 degrees to provide reconstruction of individual holograms.

In holographic reconstruction, Figure 27, a flow hologram is mixed with a flow-off hologram. The angle between the reconstruction beam and the hologram pair is set to reconstruct one of the three holograms into the CCD camera. Several of the flow-off holograms are recorded to achieve interferogram fringe configurations varying from infinite fringe to 100 waves of tilt. The three forms of interferometry analysis utilize appropriately configured interferograms. The fringe tracking (FT) method uses 20 to 50 waves of tilt depending on the strength of the wavefront distortion. The spatial Fourier transform (SFT) method requires the most tilt (80 to 100 waves) to obtain maximum spatial resolution. The phase shifting (PS) method is the most flexible and functions with tilts from zero to 100 waves. The PS method uses a plate rotation device to shift the phase between the flow and flow-off wavefronts.

The FT method, Figure 28, provides wavefront RMS and correlation measurements. The SFT and PS methods measure the wavefront phase maps directly, hence providing more direct information than the FT method. The phase map is used to compute the point spread function.

Boresight Sensor

The boresight sensor, Figure 29, uses a collimated HeNe laser beam which is directed into the optical bus. Within the optical bus, the beam is directed into the flow field and the seeker head aperture, and finally returned to the source/sensor platform. The boresight sensor is composed of a telescope and a quadrant detector. The angle measured is the ratio of the spatial deflection to the telescope focal length. The electrical sensitivity of the quadrant detector is designed to provide the required sensitivity of 10 microradians. A ± 1.0 milliradian dynamic range is achieved with an 8-bit digitizer. The sensor measures voltages during the established flow time period and is calibrated to convert voltage into angle, Figure 30.

High-Speed Point Source Imaging

High-speed imaging systems acquires point source image data at both visible (0.633 micron) and broad band mid-wave infrared (2 to 5 micron) wavelengths. Both systems acquire digitized point source image intensity distributions of the flow field degraded image of a subresolvable point source. Tare image data, recorded in the absence of flow field turbulence, will be nearly diffraction limited. It is determined solely by the aperture shape of the seeker window, and by the small amount of optical aberration (under 1/4 lambda peak-to-valley error) present in the delivery and collection optics of the lab-tunnel interface structure. Such tare image data is compared to degraded images that are collected in the presence of flow field turbulence.

The visible imager subsystem is outlined in Figure 31. An expanded, collimated HeNe laser beam is directed through the flow field and into the seeker aperture. This degraded wavefront is relayed from the tunnel test chamber and onto the sensor platform. There, the wavefront is focused onto a cooled, 512 x 512 silicon CCD array.

A high-speed scanning system is used to provide numerous images at time intervals ranging from microseconds to milliseconds. This allows more information to be acquired during the few milliseconds that the flow field is present. The scanner consists of a pair of acousto-optic beam deflectors, located in a plane that is conjugate with the seeker aperture and with the CCD camera entrance pupil. One possible acquisition format is shown in Figure 31, in which a 4 by 4 mosaic of 128 x 128 pixel images are collected on the CCD array. Time intervals and exposure durations can be adjusted based on either time averaged or instantaneous image data.

The infrared imager subsystem is designed to operate in the 2 to 5 micron wavelength regime. Radiation from a blackbody source is collimated and directed into the flow field and the seeker aperture, along with the HeNe and ruby laser beams used for the visible imager and holography instruments. Calcium fluoride/barium fluoride doublet lenses, achromatized over a 2 to 5 micron wavelength band, are used to relay the degraded wavefront and focus it onto a 128 x 128 InSb focal plane array. The InSb camera is capable of a one kilohertz frame rate. The system is shown in Figure 32.

Point source image data from both the visible and the infrared imager systems are handled similarly, Figure 33. Strehl ratio shows how peak image intensity, a parameter

that is important for effective target acquisition, decreases with increasing flow field turbulence. Encircled energy versus diameter plots show, relative to the tare image, how energy in the flow degraded image is dispersed outward and away from the center of the image. Modulation transfer function plots show how contrast or modulation depth for individual spatial frequency components of an image are decreased as image blur increases.

Radiometer/Spectrometer

The Radiometer/Spectrometer instrumentation for the LENS facility was designed to provide both high temporal broad band IR emission measurements simultaneous with moderate temporal and spectral emission measurements, respectively. The turbulent boundary layer outside of the seeker-head window for high-speed boundary layers necessitates the relatively high data acquisition rates, while the high temperatures of the boundary layer require spectral characterization. This is especially true since some seeker-head designs involve the introduction of a coolant gas flow over the seeker window. This introduction of the coolant gas and the resulting flow field chemistry is characterized by infrared emission and absorption processes due to highly excited infrared active molecular species. Computer modeling does not provide adequate quantitative results. Thus, the radiometer and spectrometer instrumentation have been designed to fulfill the system designers needs as to which wavelength bands are acceptable for seeker window/detector design.

In Figure 34, the IR radiometer subsystem overview is shown. The radiometer detector consists of a LN_2 cooled InSb photo diode 1 mm in diameter. Presently the detector geometry is a 60 degrees warm field of view with no cold filter. The maximum desired spectral band width is from 1.5 to 5.3 micron. The noise equivalent photon rate for the system is approximately 6.7×10^9 photons/sec (RMS) at 200 KHz bandwidth. The measurement bandwidth was designed for 200 KHz or less with a digitization rate up to 1 MHz (16 Bit). The measurements with the radiometer system will result in a calibrated measurement of the radiance for a user selected broad band in the MWIR in the presence of shock tunnel flow.

The data processing scheme for the IR radiometer is shown in Figure 35. For an emission measurement, the detector is sampled at rates up to 1 MHz. The voltage as a function of time is converted to radiance through previously acquired calibration curve, and an average radiance and variance of the radiance is determined for the flow period. The

power spectrum of the temporal radiance measurement will be computed and analyzed for characteristic frequency.

In Figure 36, the schematic for the spectrometer subsystem is shown. The purpose of this instrument is to measure the spectral emission and transmission of the MWIR radiation from the turbulent hot boundary layer. A 32 channel LN₂ cooled InSb detector is illuminated via a 38.1 mm diameter aperture, the IR radiation dispersed from a LiF prism. The three major MWIR atmospheric windows of 1.9 - 2.5 micron, 2.9 - 4.2 micron and 4.4 - 5.2 micron are covered. The wavelength resolution of the instrument varies from 0.29 micron at 1.5 micron to 0.1 micron at 5.25 micron. The 32 channels are sampled with a measurement bandwidth of 4 KHz (acquisition rate 15.6 KHz/channel, dedicated preamplifier for each detector element). The spectral data are acquired simultaneously with the broad band IR radiometer through aperture sharing with a beamsplitter. The spectrometer instruments will provide relative spectral radiance measurements as a function of time before flow initiation through flow termination. Treatment of the spectrometer data is outlined in Figure 37.

4.0 VALIDATION AND EVALUATION STUDIES WITH THE 2-D MODEL CONFIGURATIONS

4.1 Introduction

Following the studies to develop the LENS facility to operate under maximum total pressure and enthalpy conditions, the calibration program involving flow field surveys was begun. In this segment of the program, emphasis was placed on operating at high enthalpy conditions (12,000 ft/sec) employing for recovery pressure levels 24,000 psi. Because of the severity of these conditions, a significant effort was devoted to preventing throat and reservoir burning so that clean, particle free flow resulted in the test section. Once the facility was developed and calibrated, our attention turned to obtaining measurements on the validation models.

4.2 Objectives and Design of the Experimental Studies

The objective of this segment of the program was to obtain aerothermal and aero-optic measurements on the flat plate and 2-dimensional seeker head configurations. The first set of measurements were at low enthalpy conditions typical of those at which the HEDI configuration was run at NSWC. The major efforts, however, were focused at conditions close to ENDO LEAP design points 1 and 3; both of which were at significantly higher enthalpy levels. In fact, design point 3, represented flow conditions of 12,000 ft/sec at 100,000 ft, which potentially could produce the most severe conditions obtainable with a helium driver in the shock tunnel. In the initial phase of this effort, we sought to determine the magnitude of the effect of freestream turbulence on the aero-optical distortion measurements made with the holographic and imaging systems. For this purpose, a "flat plate configuration" was used, whose geometry was similar to the forebody containing the input beam from the aero-optic system as shown in Figure 38. The major studies was conducted with the 2-dimensional blunted wedge configuration, Figure 39 and 40, which was selected to provide aerothermal, flow field, and aero-optic measurements, Figure 41 that would be relatively easy to interpret and predict with simple and advanced CFD codes. The geometry of the nosetip and the injector position and configuration were selected to provide representative flow field configurations so that the measurements could be relatively simply applied to validate the correlations used in the design of ENDO LEAP seeker-head configurations, and so that they could be used in validation of the turbulent mixing models that are employed in the CFD codes.

4.3 Aerothermal Measurements on 2-D Seeker-Head Configurations

The initial studies with the 2-dimensional wedge configuration were conducted at the "NSWC conditions" at a Mach number of 11 and Reynolds number of 1×10^7 . The studies were conducted with nitrogen and helium coolants for blowing rates of zero and those equivalent of matched and twice matched conditions. The pressure and heat transfer measurements along the surface of the window indicated, as shown in Figures 44 and 45, that the flow was fully turbulent in the absence of blowing. The schlieren photograph of the flow and a prediction based on solutions of Navier-Stokes equations, shown in Figures 42 and 43, so a well defined recirculation region downstream of the injector whose geometry is typical of that for a turbulent boundary layer. For matched blowing, Figure 46 and 47, at this low enthalpy condition, the window is fully cooled, and can be seen in Figures 48 and 49, and the pressure distribution over the wedge is not significantly different from that without blowing. Studies to examine cooling effectiveness were then conducted at velocities of 7,200 ft/sec and 11,000 ft/sec (see Table 3) which are close to ENDO LEAP points 1 and 4. Figure 50 show the distribution of heating along the surface

Flow Parameter	"NSWC Conditions"	Test Point 1	Test Point 3
Velocity ft/sec	4850	7200	11000
Pitot Pressure psia	22 psia	37 psia	35 psia
Total Pressure psia	7800 psia	7800 psia	7800 psia
Total Temperature °R	2000 R	2000 R	2000 R
Stagnation Heating Btu/ft ² sec	48	120	370

Table 3 Shock Tunnel Flow Parameters.

for cooled (with N₂ coolant) and uncooled window configurations for the two high velocity conditions. The measurements which are shown correlated in terms of the HEDI correlation parameter in Figure 51, indicate that the effectiveness of film cooling is significantly decreased with the increase in the free stream velocity and decreased shock layer density. These same parameters also exhibit significant effect on the aero-optical performance of seeker head aperture.

4.4 AO Measurements

An initial suite of aero-optics measurement capabilities were assembled for the validation studies in the 96" HST, Figure 52. These instruments included: side view holography, seeker view holographic interferometry, boresight error and , point source imagery. In this section, the boresight sensor and the seeker view aero-optic data will be examined.

Boresight Error Measurements:

The BSE sensor signals are shown in Figure 53 for the flat-plate model. For this model, both windows are aligned with the flow in the tunnel. Therefore, wave disturbances in the optical path are minimized. Since the BSE sensor signals were digitized with a LeCroy oscilloscope, the data before the arrival of the station-7 trigger could be retained (i.e., pre-triggered mode). Also, with the extensive memory available, data signals were digitized over a long time period, 200 ms. The portion of the BSE signal that coincided with established flow was identified and analyzed for mean and fluctuating values. The mean values for channels 1 and 2 were 4.2 microradians and -6.9 microradians, respectively. Channel 1 was vertical or elevation angle, and channel 2 was horizontal or azimuth angle; these levels are essentially zero on any scale that is important to an infrared sensor. The RMS values were equally low. This stability level in the microradian range means that, for the first time, images of long duration (4 milliseconds) may be exposed in a ground test facility that are representative, or perhaps even duplicates, of those that would occur in flight.

4.4.1 Validation of Interferometry Analysis

Random Wavefront Generator

Computer codes have been developed that allow us to model the manner in which an optical wavefront is degraded due to passage through a turbulent flowfield. The purpose of such simulations is two-fold. First, it allows us to create interference patterns very similar to the holographic interferograms that are measured in real tunnel trials. With such simulated data, we can test the different interferogram analysis techniques, and verify that they are giving accurate answers. Secondly, it allows us to study the manner in which far-field point source image distributions, which are very important in evaluating seeker

performance capabilities, are affected by varying degrees of RMS wavefront error and by flowfield length scales. The simulation process, outlined in Figure 54, starts with a random, two-dimensional "white noise" distribution. This is then smoothed via two-dimensional convolutions. By adjusting the size of the convolving window, the appropriate x and y length scales (in aerodynamic parlance), or coherence lengths (in optics parlance) can be selected. The desired RMS wavefront error is adjusted simply by scaling with a multiplicative constant.

Phase Measurement

The phase map can be measured with HI through conventional fringe tracking methods or through the new and more advanced interferometry methods. The new methods offer increased spatial resolution and accuracy. Fringe tracking (FT) interferometry is a phase measurement technique in which the fringe centers are identified as contours of constant phase. After a plane wave is fit to the interferogram phase contours, the phase is determined along straight lines throughout the fringes. This is phase measurement through finite fringe interferometry. If a continuous, 2-D phase map is desired, the space between the fringes must be filled by interpolation. If the phase map contains high spatial frequency turbulence in a direction normal to the fringes, the interpolation is not satisfactory. However, fringe tracking does provide high resolution phase statistics in the direction parallel to the fringes. The information obtained along the fringes provides an excellent measurement of the phase statistics. In fact, the phase correlation function along the fringes is determined directly (Figure 55), and provides both the RMS and the integral length scale. Since the fringes in the DPHI's can be oriented in either cross aperture direction, the integral scale can be measured in both directions.

In addition to fringe tracking, other interferogram analysis techniques can be used which DPHI's can be oriented in either cross aperture direction, the integral scale can be measured in both directions. Having produced a wavefront with the desired degree of "smoothing", a corresponding fringe pattern is created by computing the interference pattern that would result from interfering the prepared wavefront with a plane wave. At this time, the fringe density, fringe orientation, and aperture diameter can be adjusted.

Spatial Fourier Transform Analysis

The SFT fringe analysis technique is very effective at providing an accurate, 2-D solution to the wavefront function, $W(x,y)$, and simultaneously provides the accompanying PSF (Figure 56). The SFT analysis is convenient and requires only a single, digitized image of the interferogram and a desktop computer of modest capability. The main requirement is that there is adequate tilt between the object and reference beams when the fringe pattern is recorded. The fringes must be nominally straight, and go from one end of the pupil to the other. Ring-like structures and fringes that curl onto themselves must be avoided. (Such fringes lead to aliasing-like conditions and prevent accurate recovery of the wavefront.)

The technique begins by computing the 2-D Fourier transform of the fringe pattern intensity distribution, $I(x,y)$. In the Fourier domain, the far-field, complex amplitude distribution of the object beam wavefront is immediately recovered. It appears as one of two sideband lobes on either side of the zero-order spike at the origin. The squared modulus of either of these two sidebands represents the point source image that would result if the flowfield-aberrated wavefront were brought to its best focus.

Next, one of the two, complex sideband structures is cut out of the larger data set, and the inverse Fourier is transformed back to the spatial domain. This complex data set also represents the object beam amplitude distribution, but in the near-field, rather than in the far-field domain.

The wavefront function, $W(x,y)$, is related to the phase function, (x,y) , by a simple multiplicative constant:

$$W(x,y) = \frac{2\pi}{\lambda} \phi(x,y)$$

To isolate the wavefront function, $W(x,y)$, the phase, (x,y) is first computed. This is accomplished by computing the arc tangent of the ratio of the imaginary field component to the real field component. This step leads to a $\pi/2$ ambiguity in (x,y) that is remedied by a special inspection algorithm that has been developed.

Following this, computations are made on the wavefront function, $W(x,y)$, in order to determine its RMS error, length scales and other parameters of interest. In summary, three methods to obtain phase maps or statistics from SPHI's or DPHI's, respectively, have been implemented and validated. The PSI and SFT methods appear well-suited for obtaining "filled-in" phase maps, whereas fringe tracking methods appear well-suited for obtaining phase statistics. For the double-exposure HI it is necessary to record holograms with fringes in each direction, so that each integral scale will be obtained. The PSI method is inherently superior to the SFT method because it utilizes three or more interferograms, achieved through manipulation of the double-plate hologram reconstruction device. This is a distinct advantage for less than ideal or noisy interferograms which normally occur in wind tunnel environments. A quantitative comparison of these analyses for aero-optic evaluation is now presented.

Phase Shifting Interferometry

PSI is a very powerful wavefront analysis technique that allows the interrogation of wavefronts having large (several waves) peak-to-valley errors, and with much higher spatial resolution than is afforded by other techniques. The price paid for this enhanced robustness is that more hardware is required in PSI setup, and that three or more phase shifted interferograms of the same wavefront must be recorded and digitized (Figure 57).

In the PSI setup, it is necessary to have the ability to precisely shift the phase of the reference beam relative to the object beam, typically by 90 degrees. Interferograms are recorded at three, four, or five, different amounts of phase shift, depending on which specific PSI algorithm is used. If the three different intensity distributions are known as $A(x,y)$, $B(x,y)$, and $C(x,y)$, then the phase, (x,y) , is obtained from:

$$\phi(x,y) = \tan^{-1} \frac{C(x,y) - B(x,y)}{A(x,y) - B(x,y)}$$

As in the Fourier analysis technique, it is necessary to correct the $/2$ ambiguities that arise from the arctangent calculation. Then, it is necessary to subtract the linear tilt components. This must be done before the wavefront's RMS error is computed.

Various types of instrumentation are used to effect the phase shifting. Often, it is done by using piezoelectric mirrors. In this case, it was done by precision rotation of the double-holographic plate holder.

4.4.2 Data Analysis

Figures 58 and 59 show data from the CUBRC 96" tunnel, run number 46, with the two dimensional wedge seeker model in place. Nitrogen coolant was used, and the interferogram aperture corresponds to a 50 mm window aperture. Single, holographic exposures were made with the pulsed ruby laser beam (20 nanosecond pulse duration) of both non-flow, or tare, and flow conditions. To produce the interferograms, both plates were placed together in a holder and illuminated with a single reconstruct beam. Simultaneously, both the tare and the flow degraded wavefronts are reconstructed, which interfere and produce the fringe patterns.

For the spatial Fourier transform analysis, the tare exposure reference beam angle is adjusted such that an adequate number of fringes, roughly 60 to 80, are present in the interferogram. (interferograms with a large number of fringes cannot be easily reproduced in print. The interferograms shown in figures 58 and 59 are of coarser fringe density, in order that they can be reproduced with some clarity. The interferograms shown in the figures are not the actual intensity distributions that were analyzed.) The reconstruction optics are carefully adjusted such that the reconstructed interferogram is uniformly intense at the CCD camera, and then the image is digitized. This digitized intensity distribution is then analyzed by the SFT analysis software, yielding the reconstructed wavefront shown in Figure 58. The rms wavefront error computed from the SFT solution for the run 46 wavefront is .36 waves.

At the same time that interferograms are digitized for SFT analysis, additional, phase shifted interferograms are digitized for phase shifting analysis. A set of three such interferograms, having the required 90 degree phase shift relative to one another, are shown in Figure 59. Such interferograms were analyzed to produce a reconstructed wavefront having an rms error of .38 waves.

The discrepancy between the SFT and the PSI solutions for the reconstructed wavefront rms error from run 46, .36 and .38 waves, respectively, is roughly 5%. Such a discrepancy is expected, and is in keeping with the random intensity fluctuations in the

interferogram data due to laser speckle, coherent scattering from dust particles, and electronic noise from the CCD camera and digitizer. At this time, we are conducting a validation study that will permit us to specify with greater accuracy the uncertainty, or error, that should accompany any reported calculations of the reconstructed wavefront, $W(x,y)$, and its rms error. The techniques for simulating flowfield aberrations, as described above, are being expanded so as to include intensity noise in the interferograms, and to characterize how such noise affects the wavefront restoration accuracy.

Comparison of Nitrogen and Helium Coolants

The most important aspect of high-enthalpy, aero-optics is the energetic state of the gas which flows from the shock layer over the seeker window. At high enthalpies, the incident gas has high velocity and temperature and low density.

The function of the window coolant is to isolate this energetic shock layer gas from the window. Nitrogen has been the coolant gas which has received the most attention; however, recently as high enthalpy conditions have become a requirement, alternative coolants, principally helium, have been considered. For nitrogen coolants, the gas is injected at low velocity and temperature and high density. In which case, the shock layer/coolant gas mixing layer has strong velocity shear and large density change. This condition results in strong turbulence, density fluctuation, and optical distortion. The use of helium gas as a coolant vastly improves the optical performance. For helium coolant, the gas is injected at high velocity and low density and temperature. In this case, the shear layer/coolant gas mixing layer exhibits weak velocity shear and minimal density change, resulting in weak turbulence, density fluctuation, and optical distortion. Helium also exhibits superior cooling performance. Therefore, helium appears to be the coolant of choice.

Runs 46 and 47 were performed, to provide a preliminary comparison of nitrogen and helium, respectively. The phase maps for these two conditions are shown in Figure 60. The rms wavefront distortions are .38 and .31 waves for nitrogen and helium, respectively. Examination of the structure and spatial frequency content of phase maps reveals that the nitrogen case exhibits a scale length near the turbulence dimension of 2 - 5 mm, and further that the distortion is present throughout the aperture. Whereas for helium coolant, the dominant frequencies are somewhat larger, but more importantly the larger scale distortions are not seen throughout the aperture.

These observations suggest that helium coolants may provide superior imagery because of the lower magnitude and larger scale of the wavefront distortion.

5.0 SUMMARY AND CONCLUSIONS

Development, calibration and validation studies have been conducted in the LENS facility over the past year to bring the facility and associated aero-thermal and aero-optical instrumentation to the capability of operating at velocities up to 4 km/sec at altitudes down to 30 km. A model support and optical bench system and suite of aero-thermal and aero-optical instrumentation have been developed for seeker head aperture evaluation. An aggressive program was successfully conducted to develop thick double diaphragm technology, address severe throat and reservoir heating problems, and construct a fast acting throat valve which survives under very high enthalpy conditions. Validation studies employing a simple seeker head aperture configuration are being conducted to validate the performance of the LENS facility and the aerothermal and aero-optical instrumentation developed for seeker head evaluation. Aerothermal studies have been conducted to examine window cooling effectiveness at velocities up to 13000 ft/sec and measurements made in these studies have been compared with similar measurements at lower velocities, simple predictions and correlation techniques and computer simulations.

References

1. Large Energy National Shock Tunnel (LENS) Description and Capabilities, Calspan-UB Research Center, February 1991.
2. M.S. Holden, "Ground Test Facilities and Instrumentation for Aerothermal and Aero-Optical Studies of Hypersonic Interceptors," Calspan-UB Research Center.

FIGURES AND TABLES

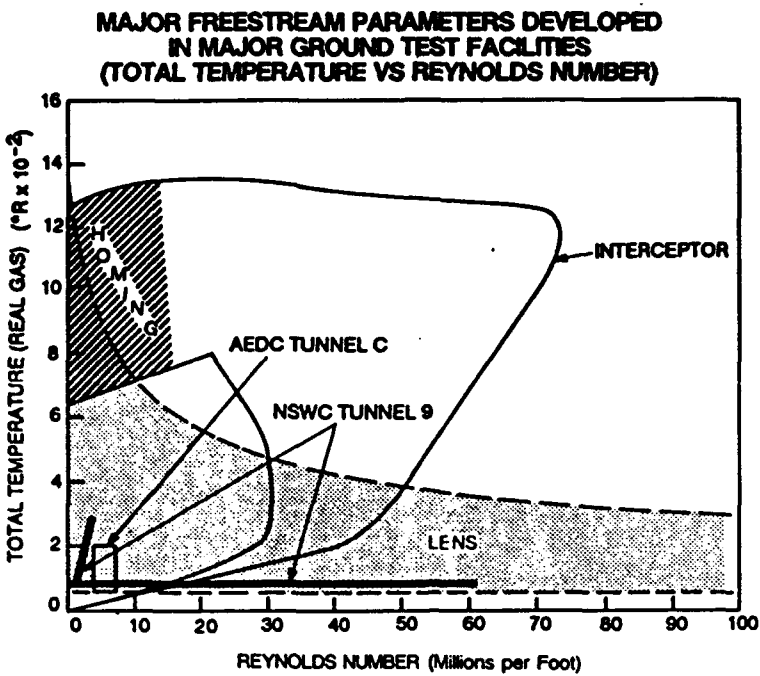


FIGURE 1 TOTAL TEMPERATURE/REYNOLDS NUMBER CAPABILITIES OF THE LENS AND CONTEMPORARY GROUND TEST FACILITIES

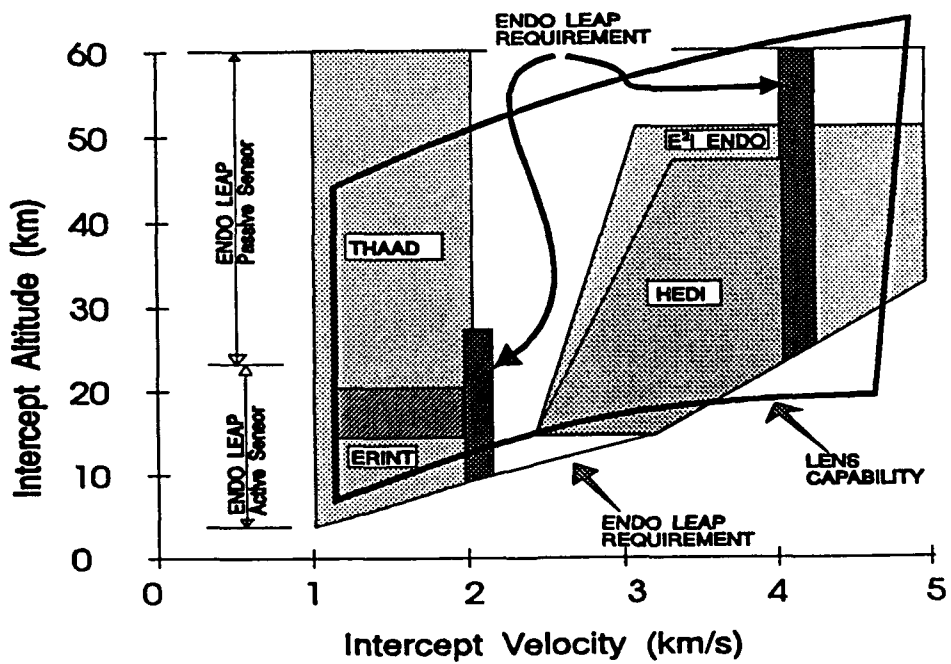


FIGURE 2 INTERCEPTOR PERFORMANCE ENVELOPE AND LENS FACILITY PERFORMANCE

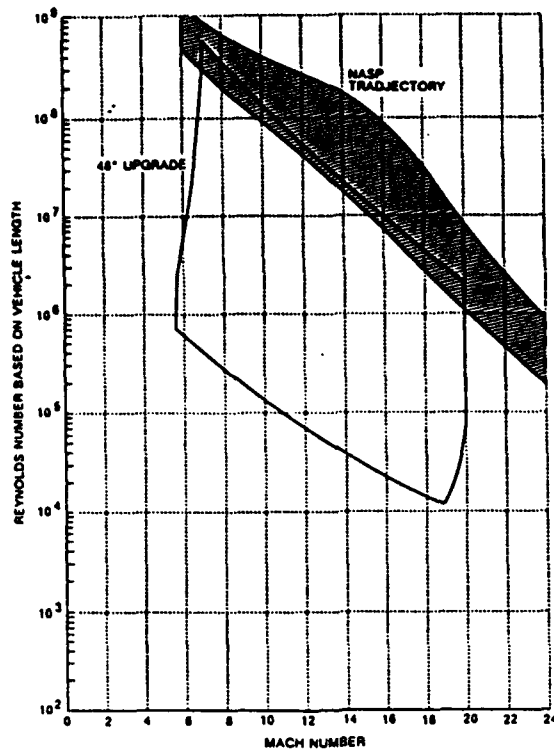


FIGURE 3 MACH NUMBER/REYNOLDS NUMBER CAPABILITIES FOR LENS FACILITY

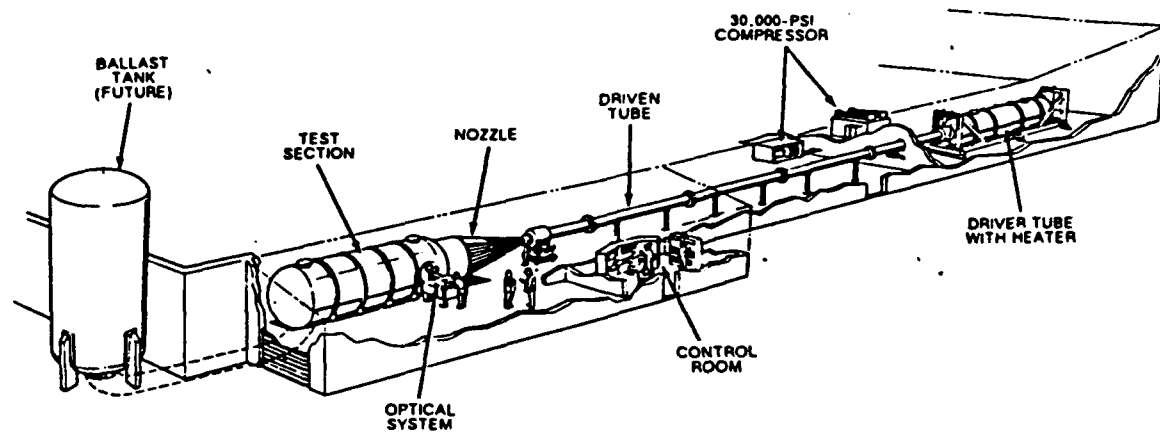


FIGURE 4 PHYSICAL LAYOUT OF LARGE ENERGY NATIONAL SHOCK (LENS) TUNNEL

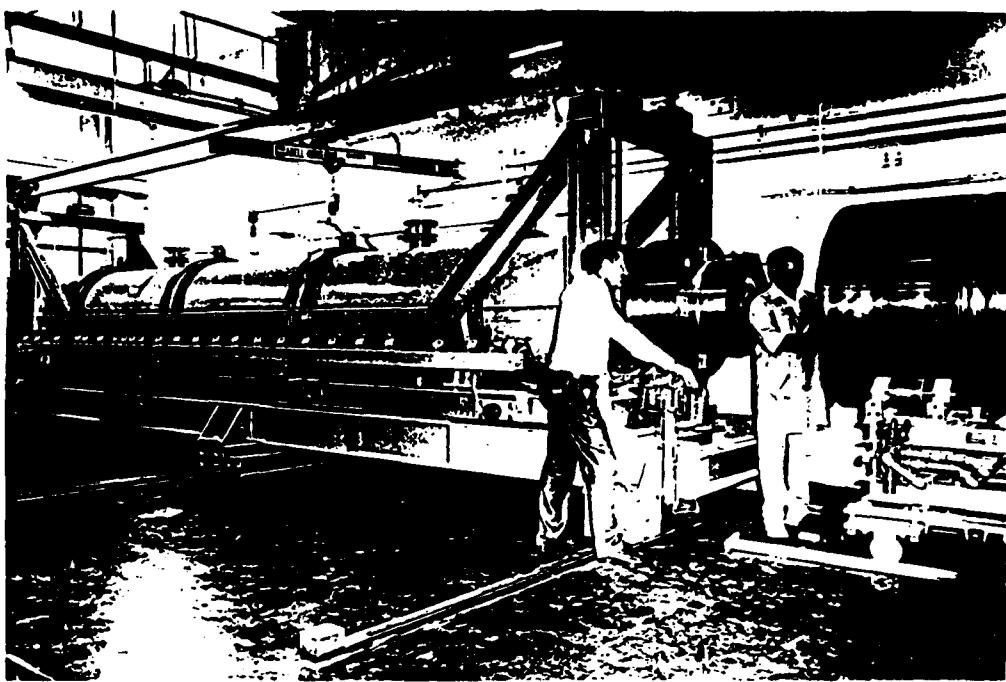


FIGURE 5 DRIVER AND DOUBLE DIAPHRAGM SECTION OF THE LENS
FACILITY



FIGURE 6 STAINLESS STEEL DIAPHRAGM FROM THE LENS FACILITY

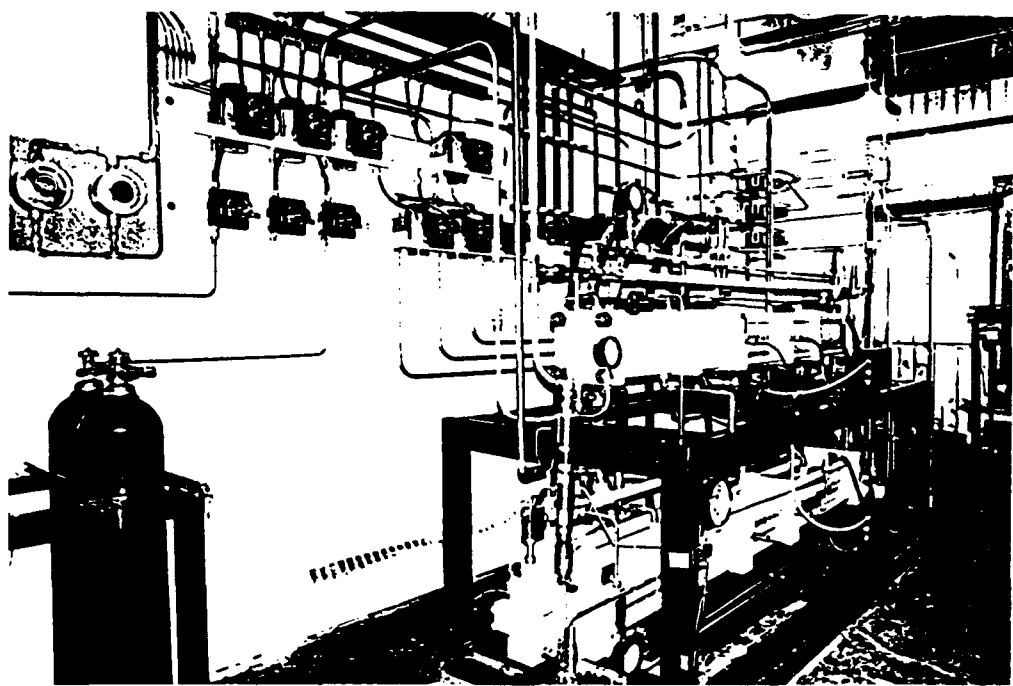


FIGURE 7 HIGH SPEED COMPRESSOR SYSTEM

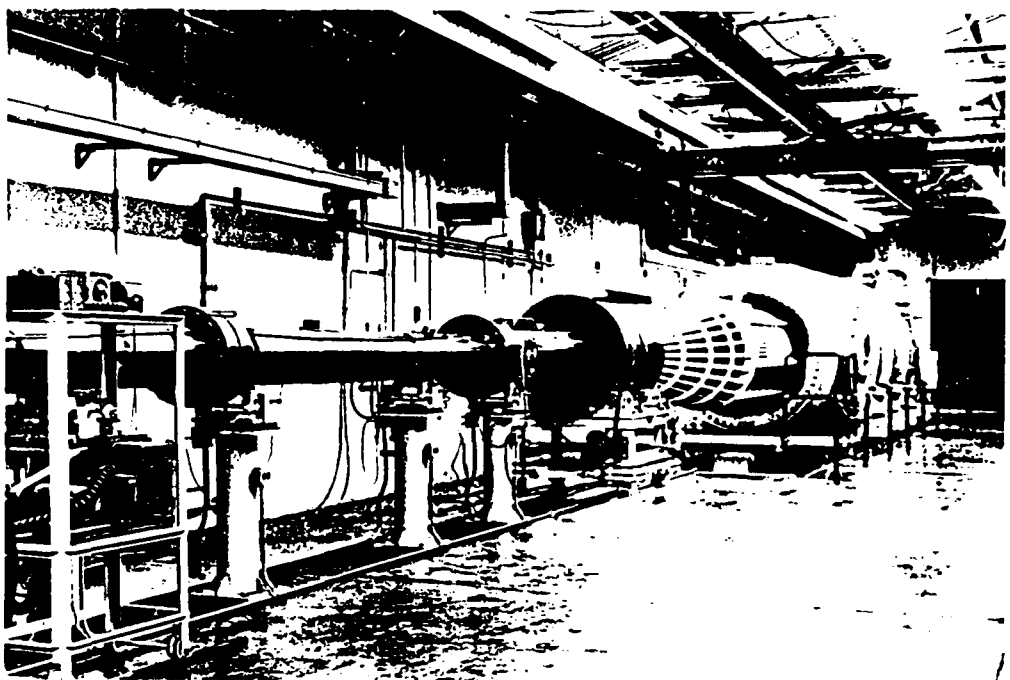


FIGURE 8 DRIVEN TUBE AND NOZZLE SECTION OF THE LENS FACILITY

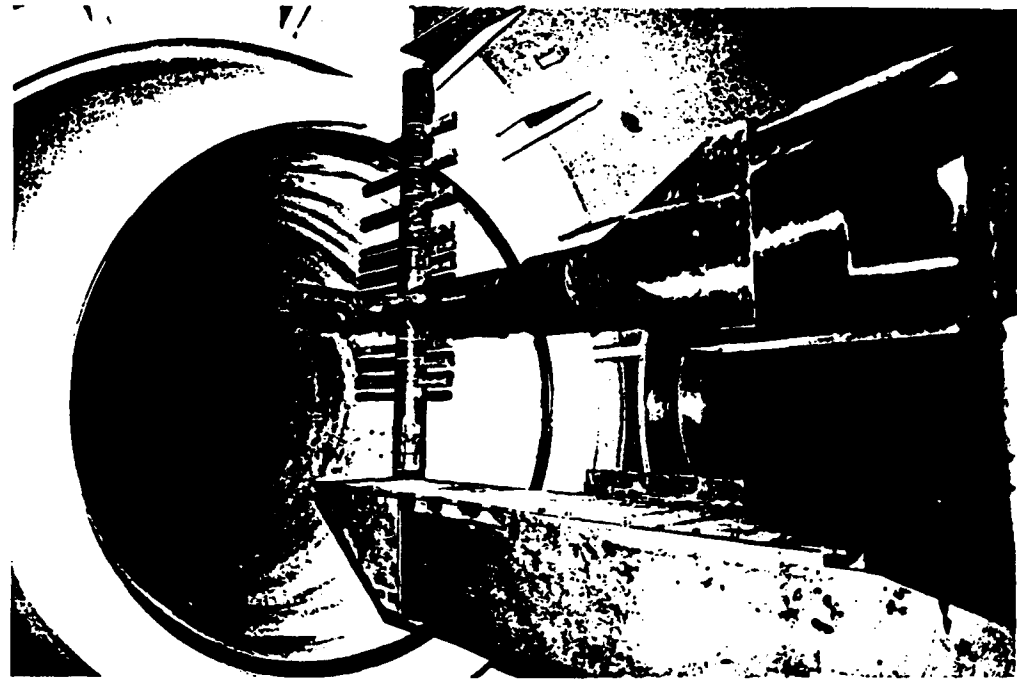


FIGURE 9 SURVEY RAKE IN LENS FACILITY

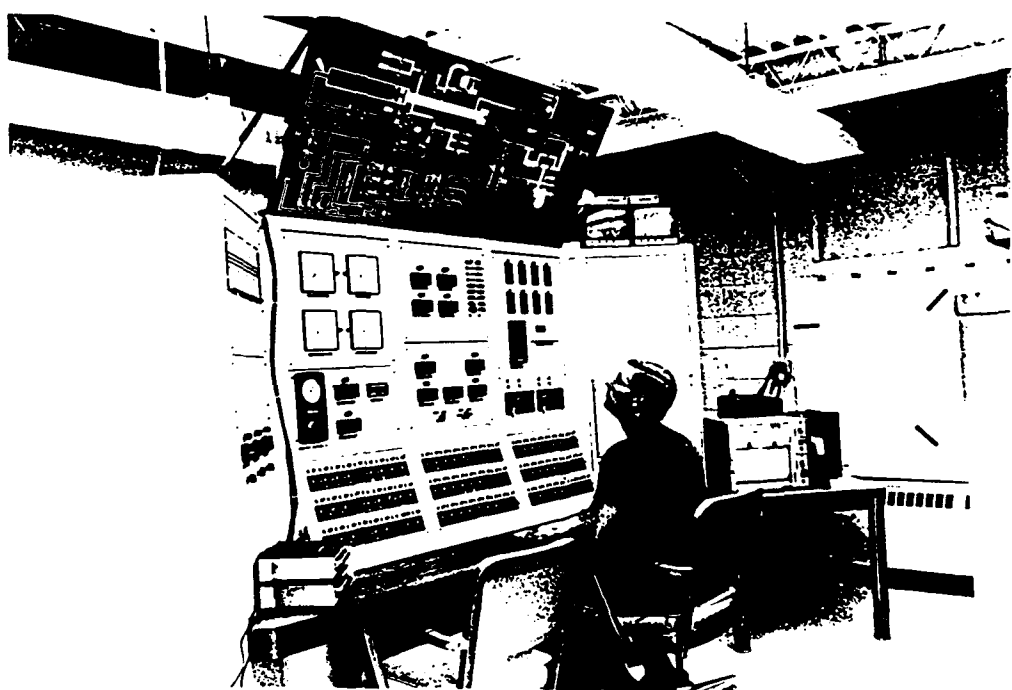


FIGURE 10 - CONTROL PANEL FOR THE LENS FACILITY

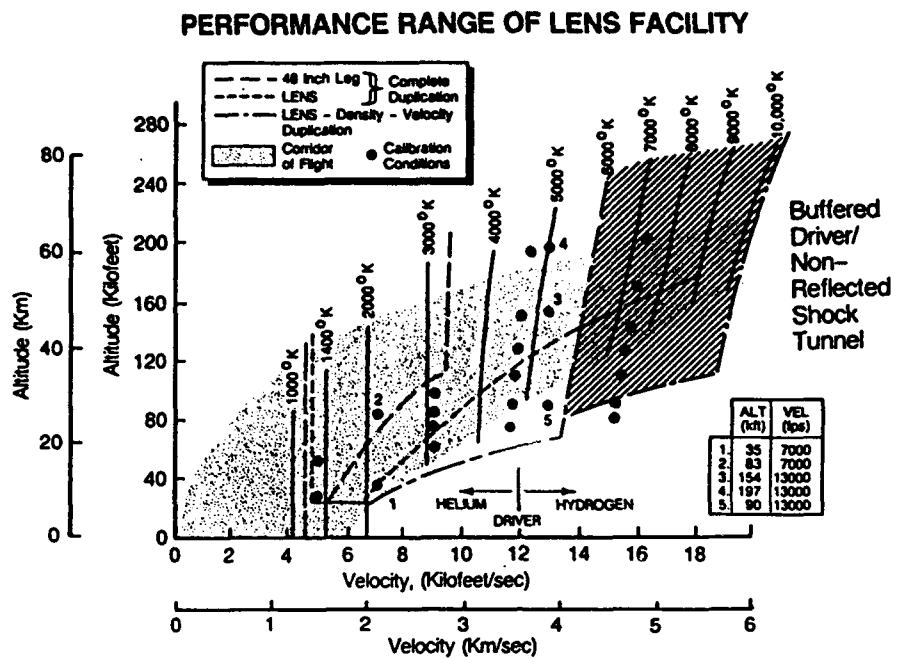


FIGURE 11 - CALIBRATION POINTS FOR THE LENS FACILITY

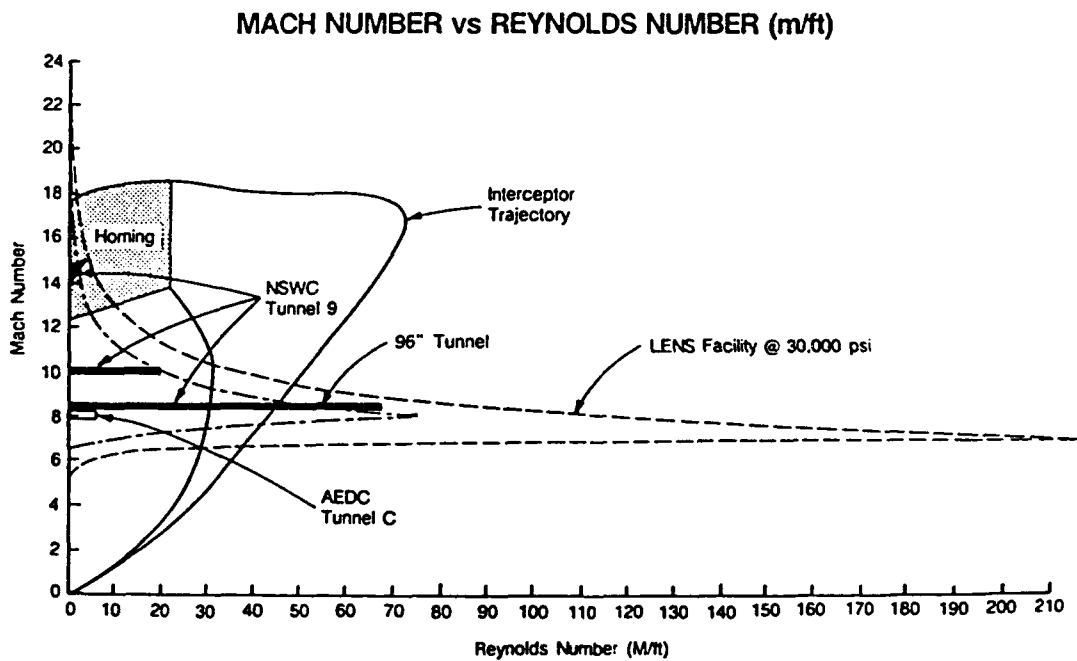


FIGURE 12 - COMPARISON BETWEEN MACH NUMBER, REYNOLDS NUMBER CAPABILITIES OF THE LENS FACILITY

TEMPERATURE PROFILE AT THE EXIT

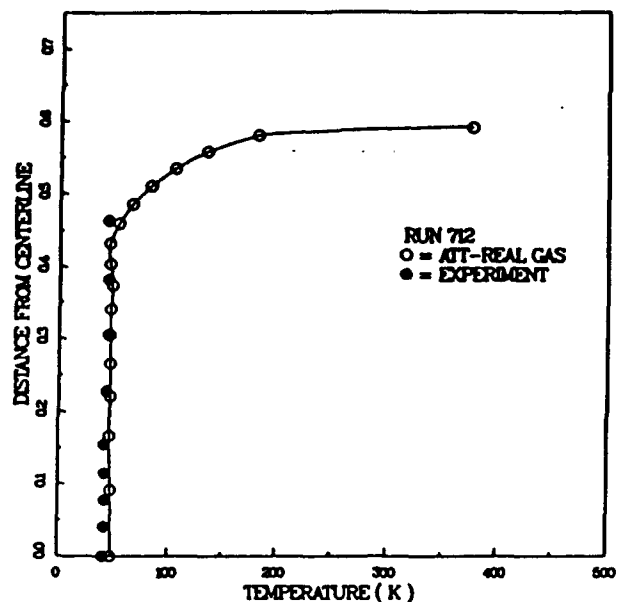


FIGURE 13 TEMPERATURE DISTRIBUTION AT EXIT PLANE OF THE NOZZLE

MACH NUMBER RATIO

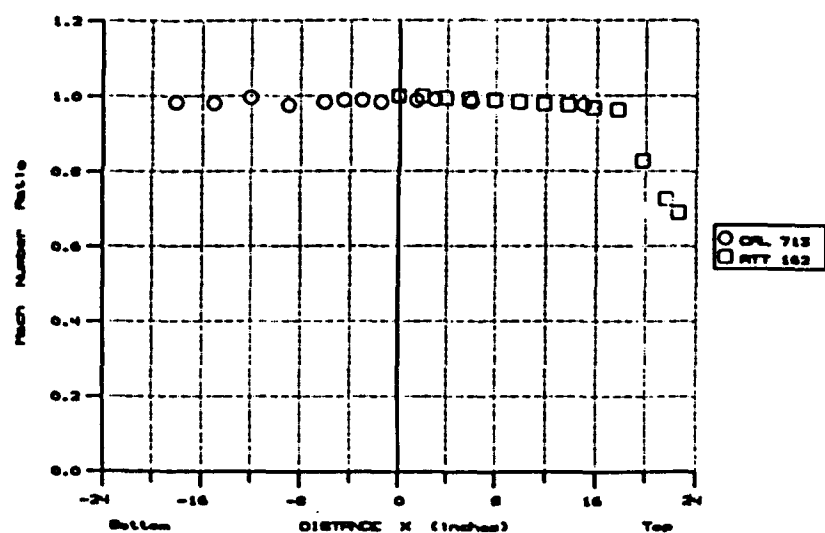


FIGURE 14 MACH NUMBER DISTRIBUTION ACROSS EXIT PLANE

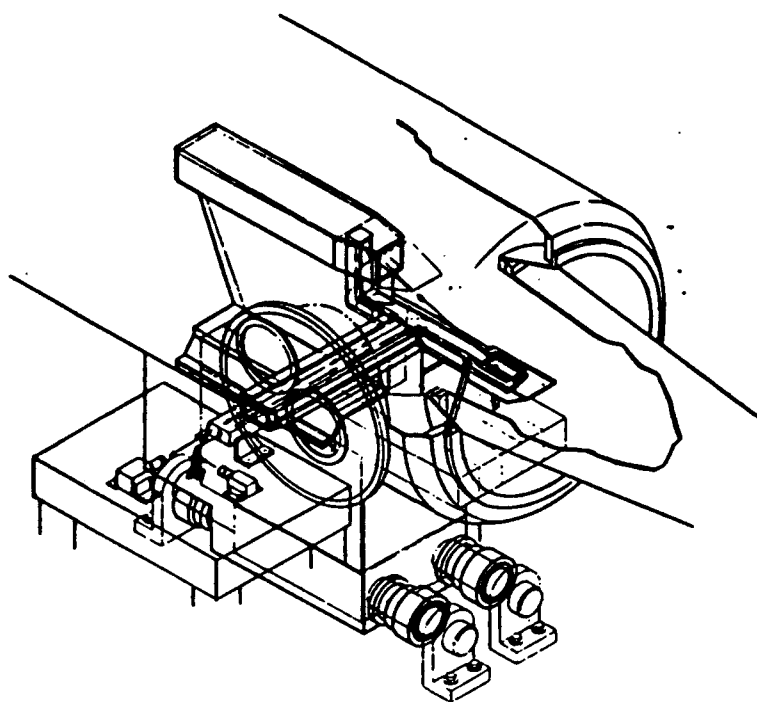


FIGURE 15 MODEL SUPPORT AND OPTICAL BENCH SYSTEM

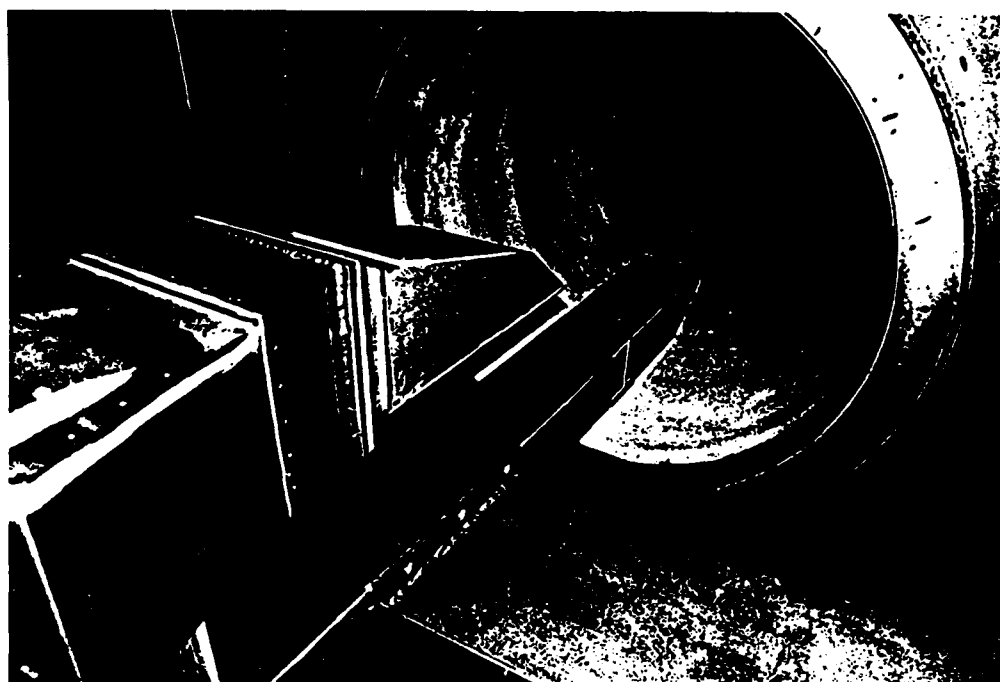


FIGURE 16 - FLAT PLATE MODEL

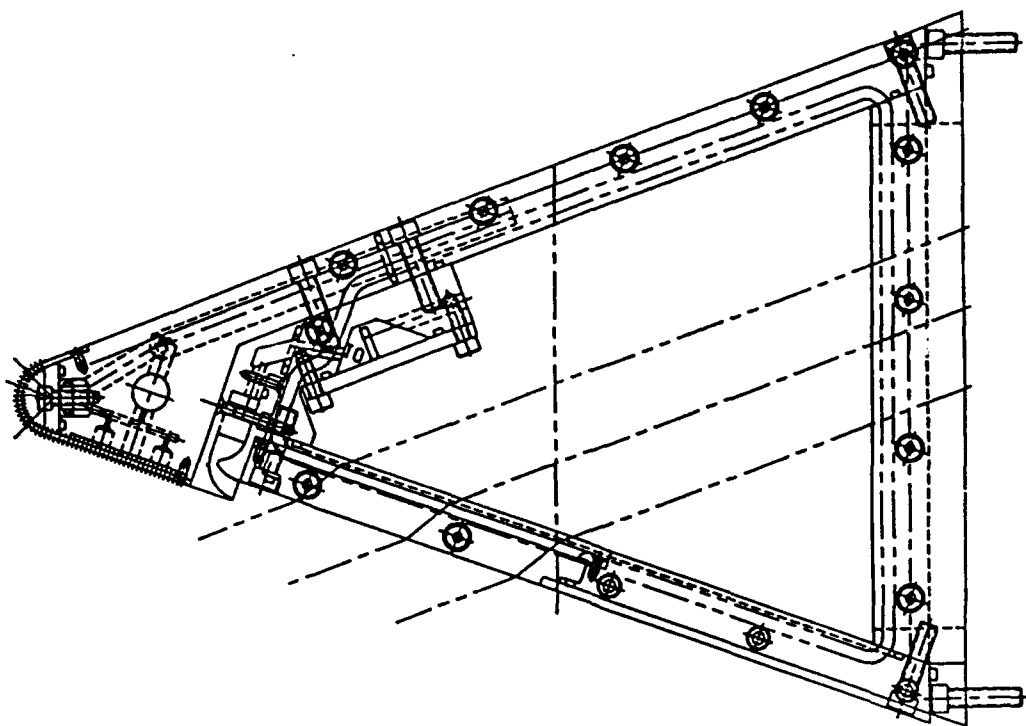
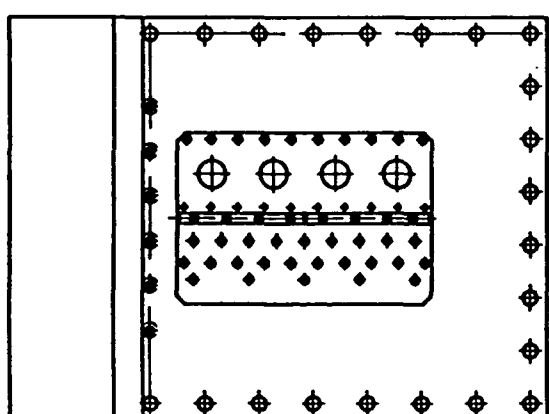
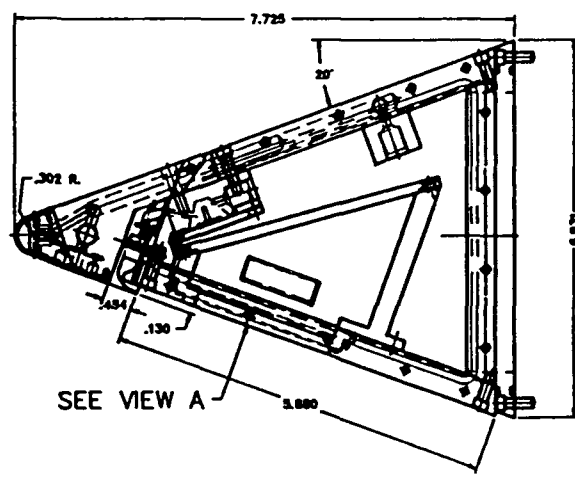


FIGURE 17 - SCHEMATIC SHOWING 2D MODEL WITH OPTICAL WINDOW



VIEW A



2-D MODEL/INSTRUMENTATION INSERT

FIGURE 18 - SCHEMATIC DIAGRAM OF 2D WEDGE MODEL

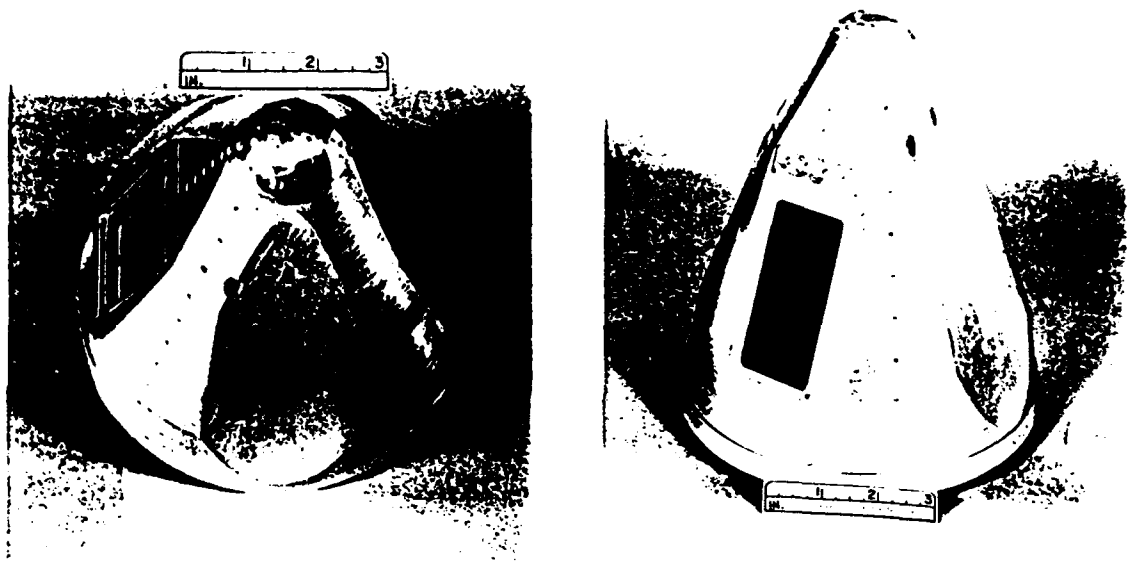


FIGURE 19 - PHOTOGRAPHS OF 3-D OF TRICONIC SEEKER HEAD CONFIGURATION

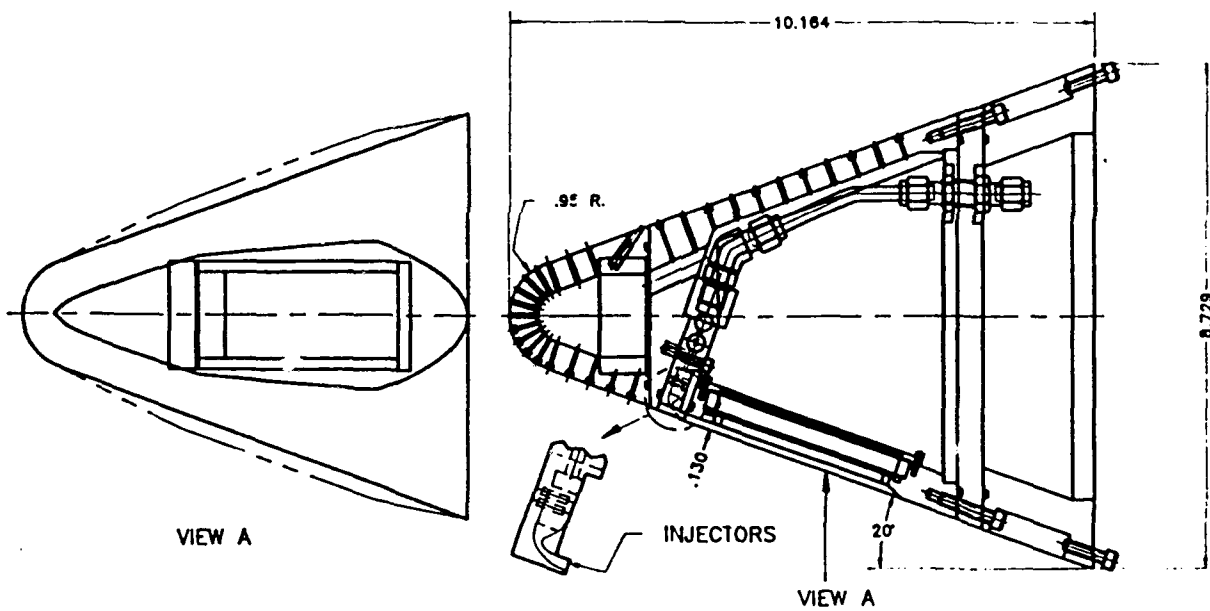


FIGURE 20 - SCHEMATIC DIAGRAM SHOWING WINDOW COOLING FOR TRICONIC CONFIGURATION

TABLE 1 AEROTHERMAL INSTRUMENTATION - SURFACE AND FLOWFIELD

SURFACE INSTRUMENTATION	FLOWFIELD INSTRUMENTATION
<ul style="list-style-type: none"> • HEAT TRANSFER <ul style="list-style-type: none"> • Thin Film Gages • Gas Cap Radiation Gages • Calorimeter Gages • Coaxial Gages • PRESSURE <ul style="list-style-type: none"> • PCB • Kulites • SKIN FRICTION <ul style="list-style-type: none"> • Force Balance - Accⁿ Comp. • RADIATION AND ELECTRON DENSITY <ul style="list-style-type: none"> • Gas Cap Radiation Gages • Flush Electrostatic Probes 	<ul style="list-style-type: none"> • INTRUSIVE <ul style="list-style-type: none"> • Pitot Pressure Rake • Total Temperature Rake • Hot Film Rake • Ion Probes • Gas Samplers • Total Enthalpy • NON-INTRUSIVE <ul style="list-style-type: none"> • Electron Beam • Laser Induced Fluorescence (LIF) • Absorption Spectroscopy • Microwave Interferometry

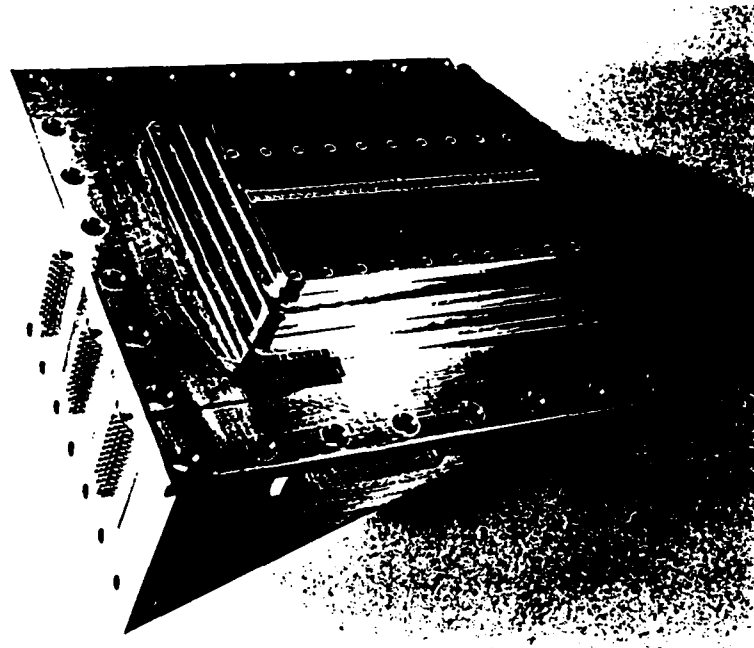


FIGURE 21 2D WINDOW INSTRUMENTATION WINDOW INSERT CONTAINING HEAT TRANSFER AND PRESSURE INSTRUMENTATION

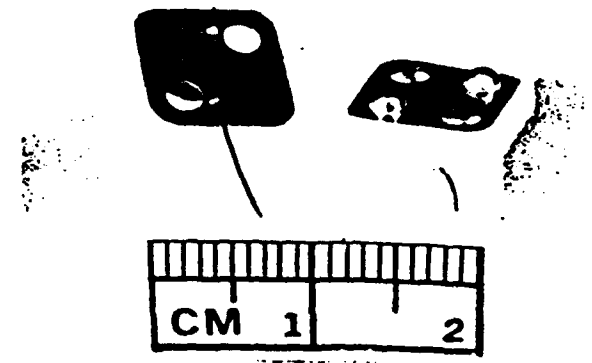


FIGURE 22 TYPICAL CALORIMETER INSTRUMENTATION

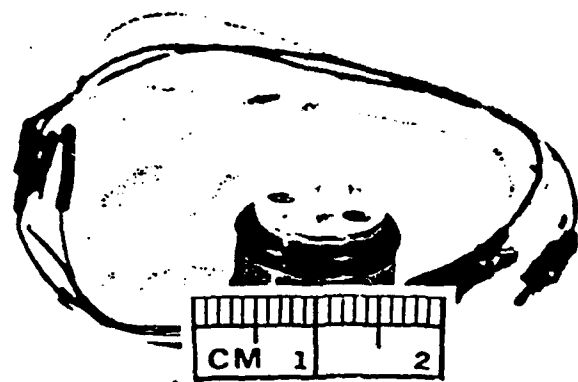


FIGURE 23 TYPICAL SKIN FRICTION INSTRUMENTATION

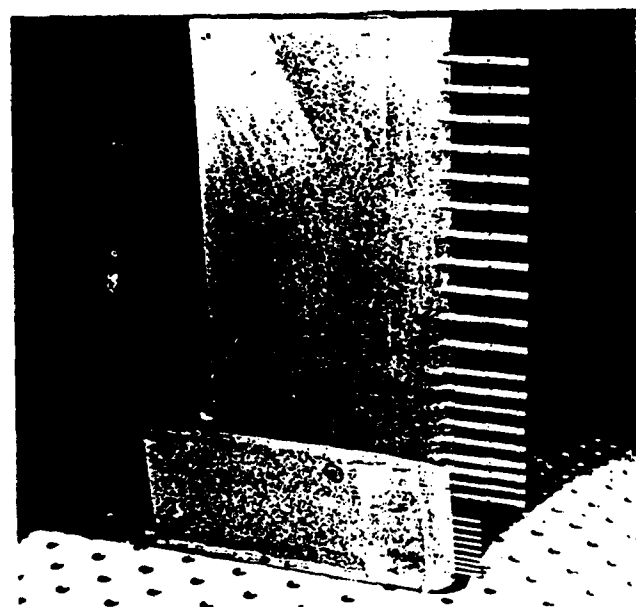


FIGURE 24 PITOT PRESSURE AND TOTAL TEMPERATURE SURVEY RAKE

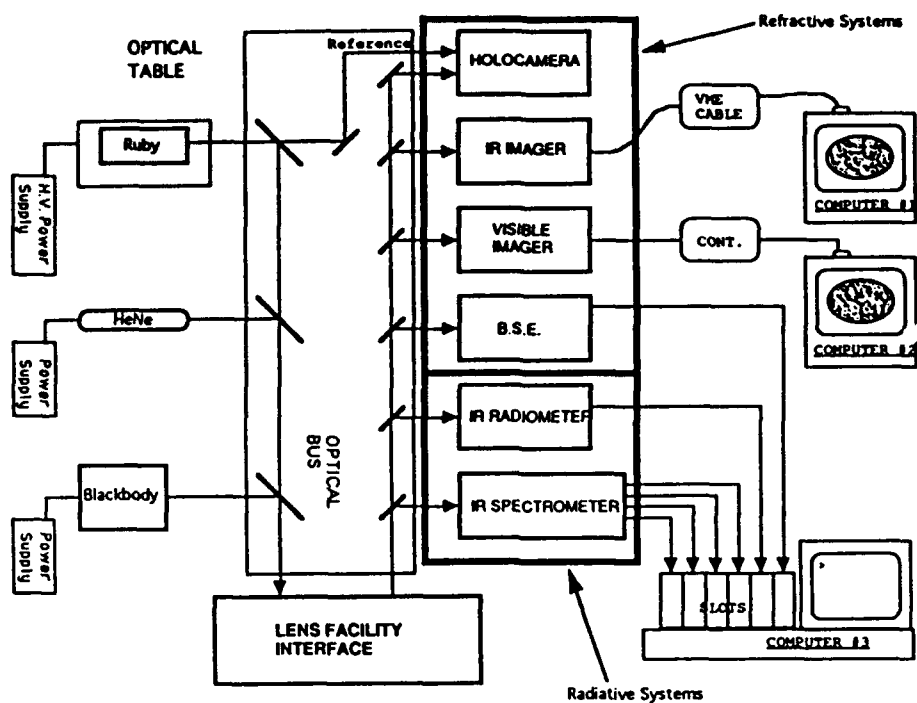


FIGURE 25 AERO-OPTIC EVALUATION CENTER
INSTRUMENTATION SUITE

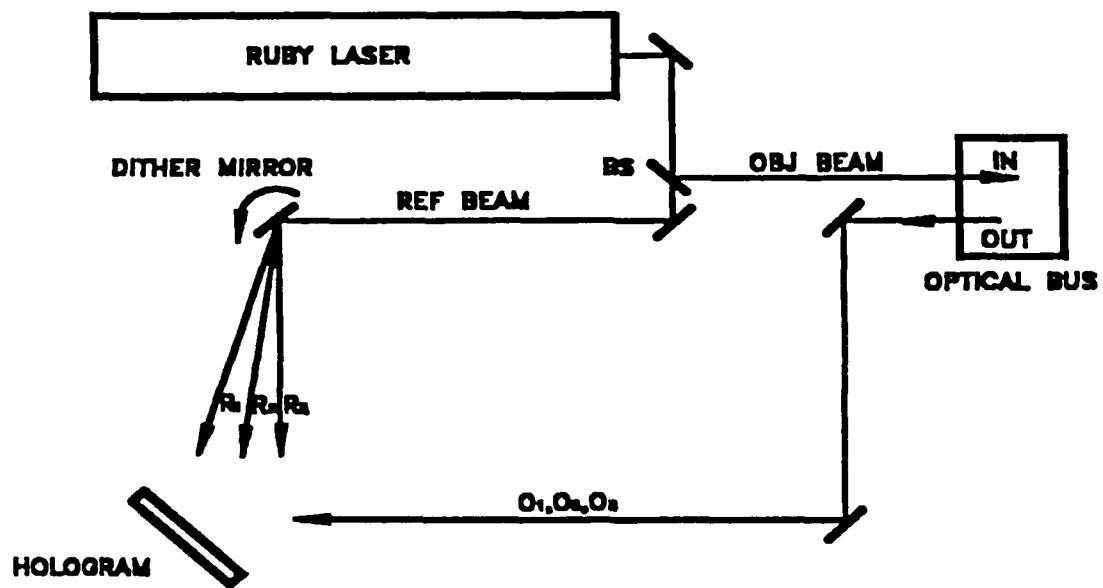


FIGURE 26 HOLOGRAPHIC INTERFEROMETRY

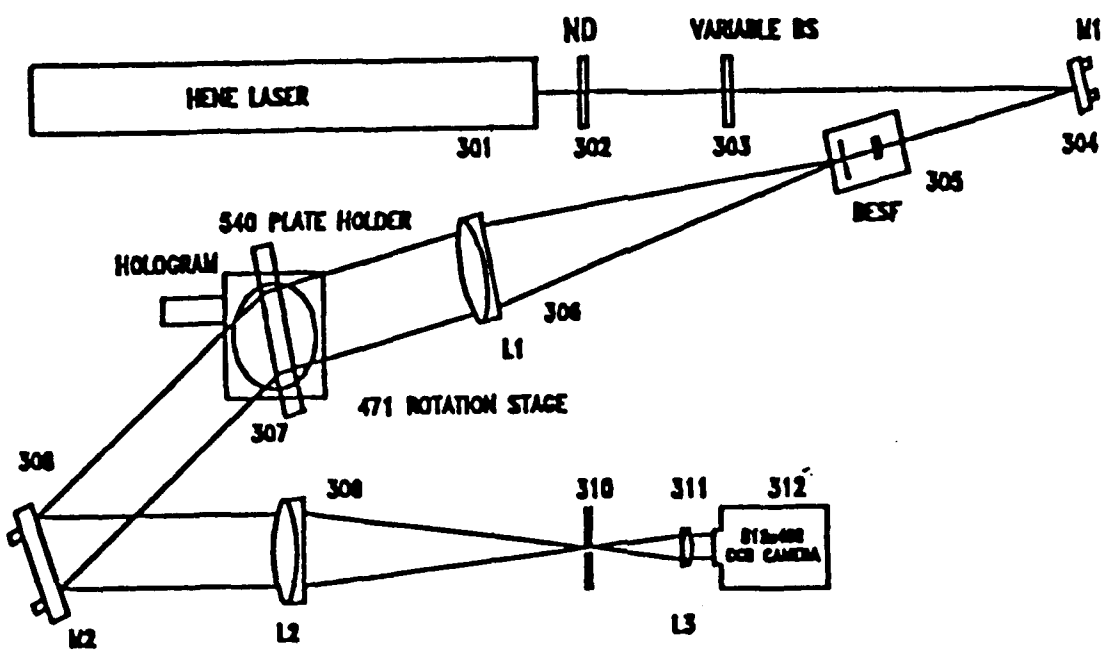


FIGURE 27 HOLOGRAPHIC RECONSTRUCTION

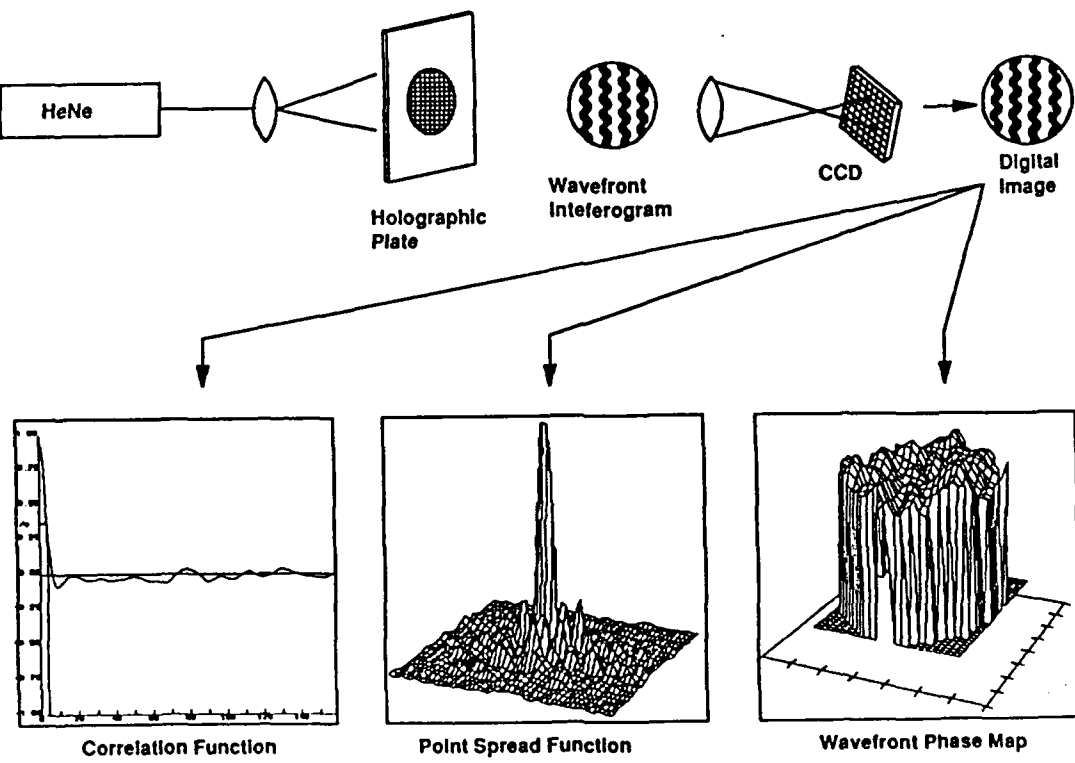


FIGURE 28 HOLOGRAPHY DATA PROCESSING

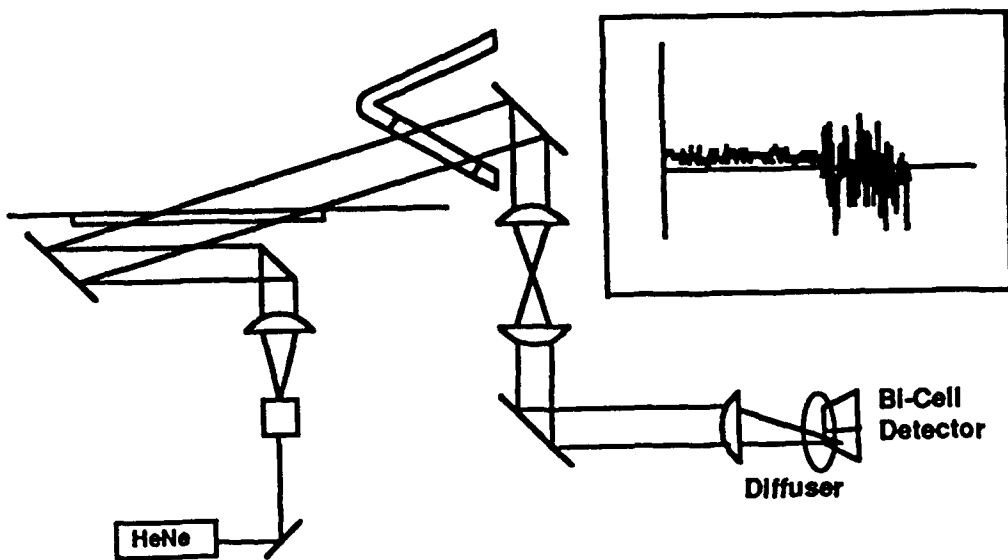


FIGURE 29 BORESIGHT ERROR SENSOR

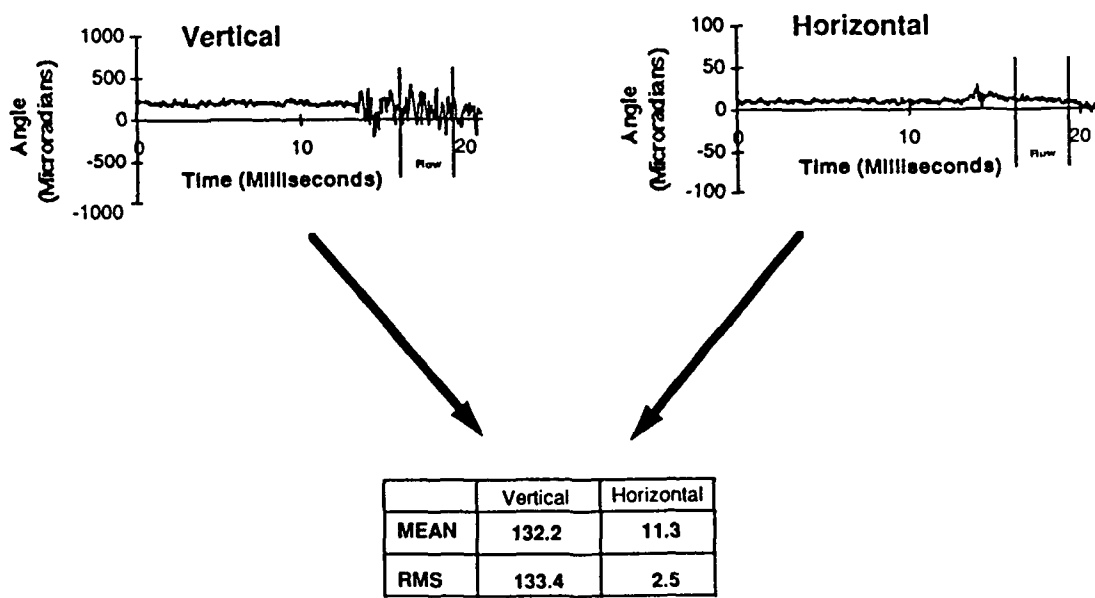


FIGURE 30 BORESIGHT ERROR DATA PROCESSING PICTORIAL

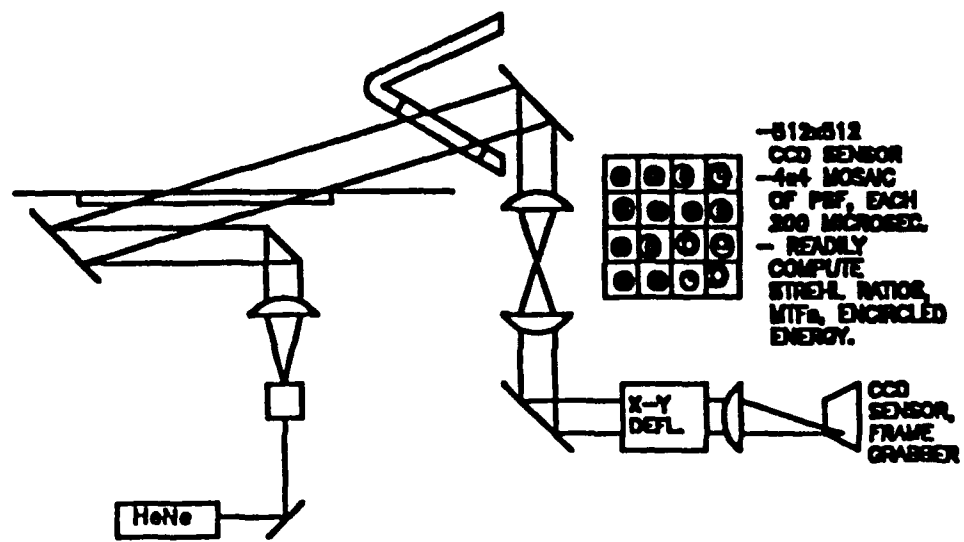


FIGURE 31 VISIBLE POINT SOURCE IMAGERY

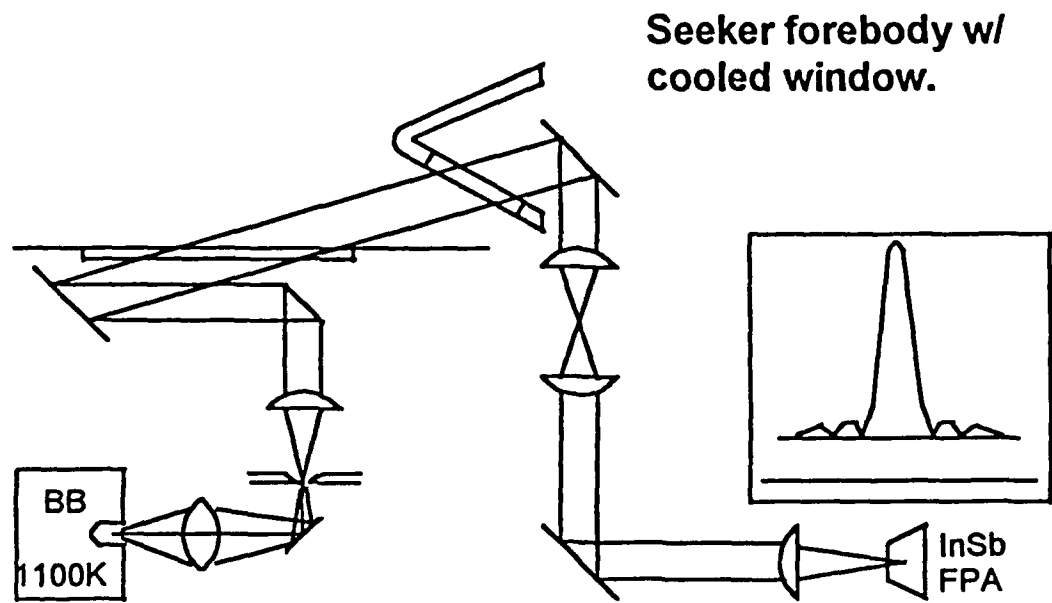
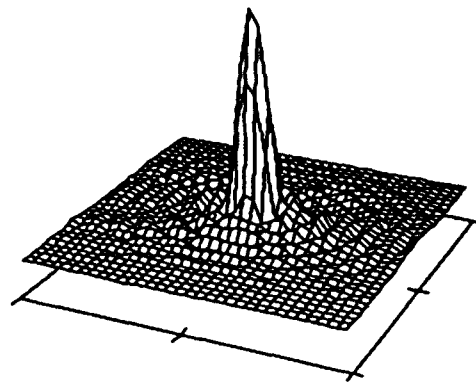
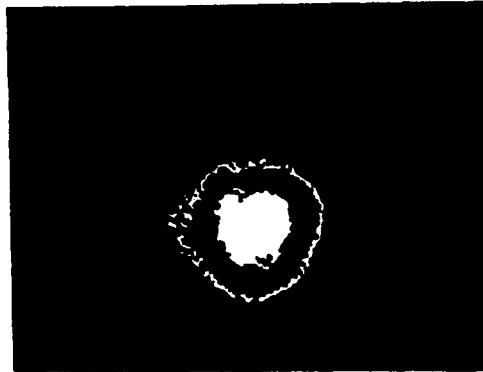


FIGURE 32 MWIR IMAGERY

Acquisition, Display and Pre-Processing



Analysis: Encircled Energy, Strehl Ratio and MTF

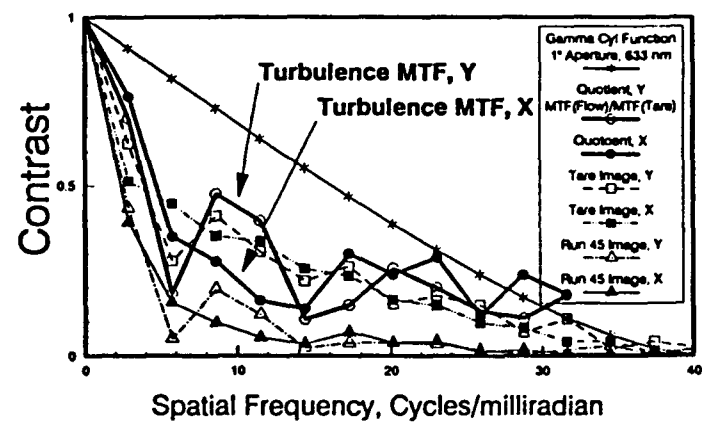
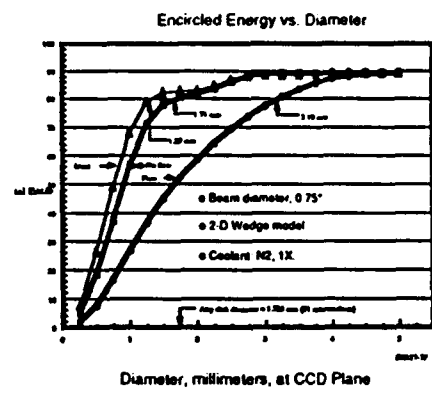


FIGURE 33 VISIBLE IMAGER DATA PROCESSING PICTORIAL

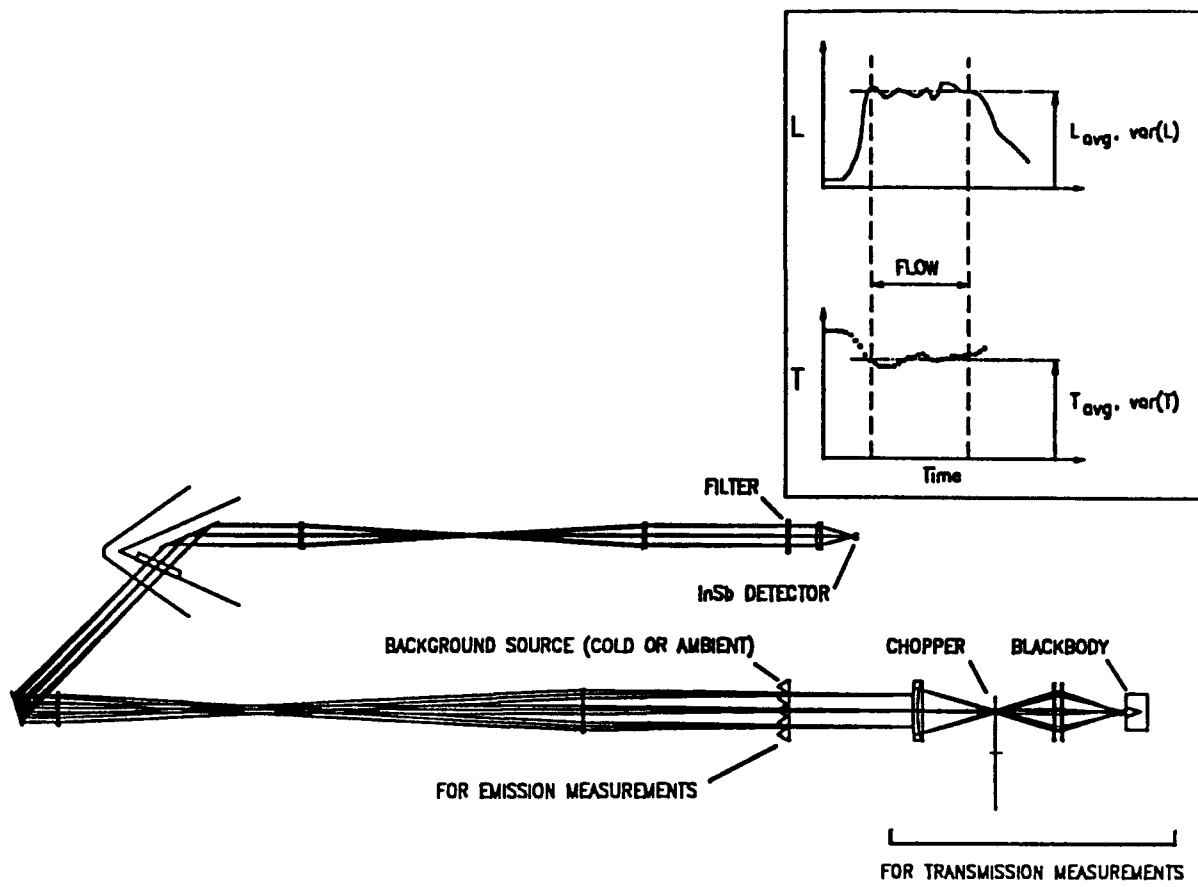


FIGURE 34 IR RADIOMETRY

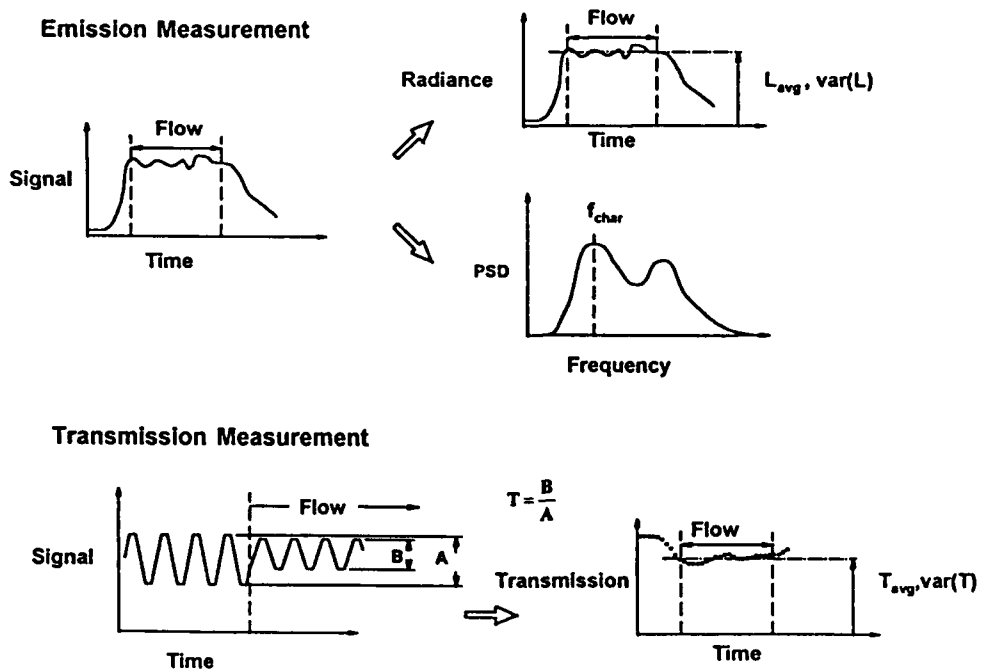


FIGURE 35 IR RADIOMETER DATA PROCESSING PICTORIAL

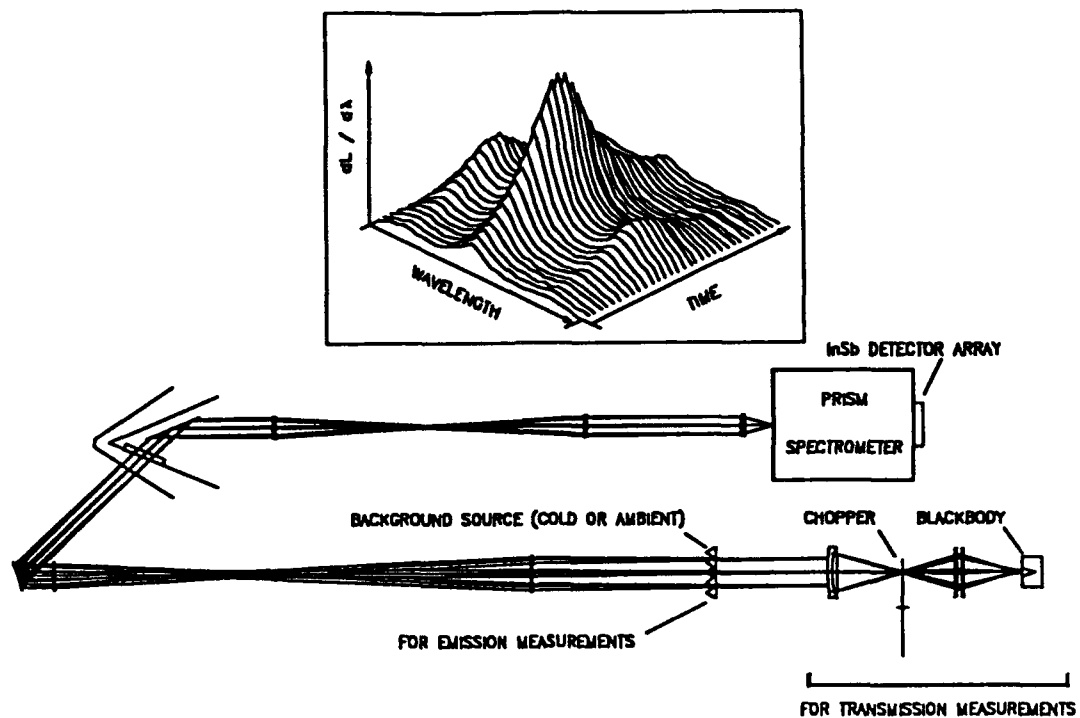


FIGURE 36 IR SPECTROMETRY

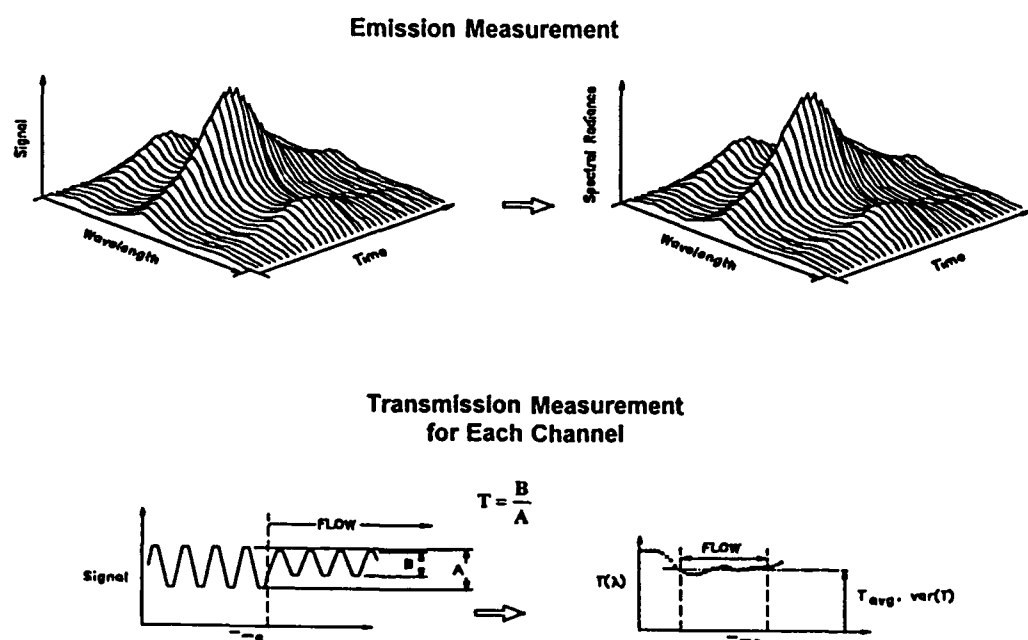


FIGURE 37 IR SPECTROMETER DATA PROCESSING PICTORIAL

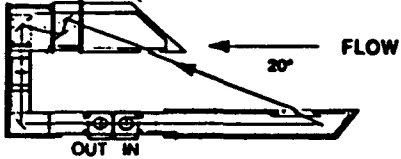
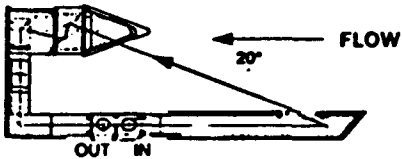
FLAT PLATE	2D WEDGE
	
<ul style="list-style-type: none"> • FLAT PLATE MODELS ALIGNED WITH FLOW • AERO-OPTIC INSTRUMENT SIGNALS DEPICT TUNNEL BACKGROUNDS: <ul style="list-style-type: none"> - TURBULENCE - REFRACTION - JITTER • OPTICAL APERTURE: 50 MM DIAMETER 	<ul style="list-style-type: none"> • BLUNT 2-D WEDGE, ($2\theta = 40^\circ$) • TRANSPIRATION COOLING: NOSE AND FOREBODY • FILM COOLED RECESSED WINDOW • COOLANT NOZZLE: <ul style="list-style-type: none"> - HEIGHT = 0.2 INCHES - MACH NUMBER = 3.0 • OPTICAL APERTURE: 50 MM, DIAMETER

FIGURE 38 SCHEMATIC OF FLAT PLATE AND 2D WEDGE CONFIGURATIONS

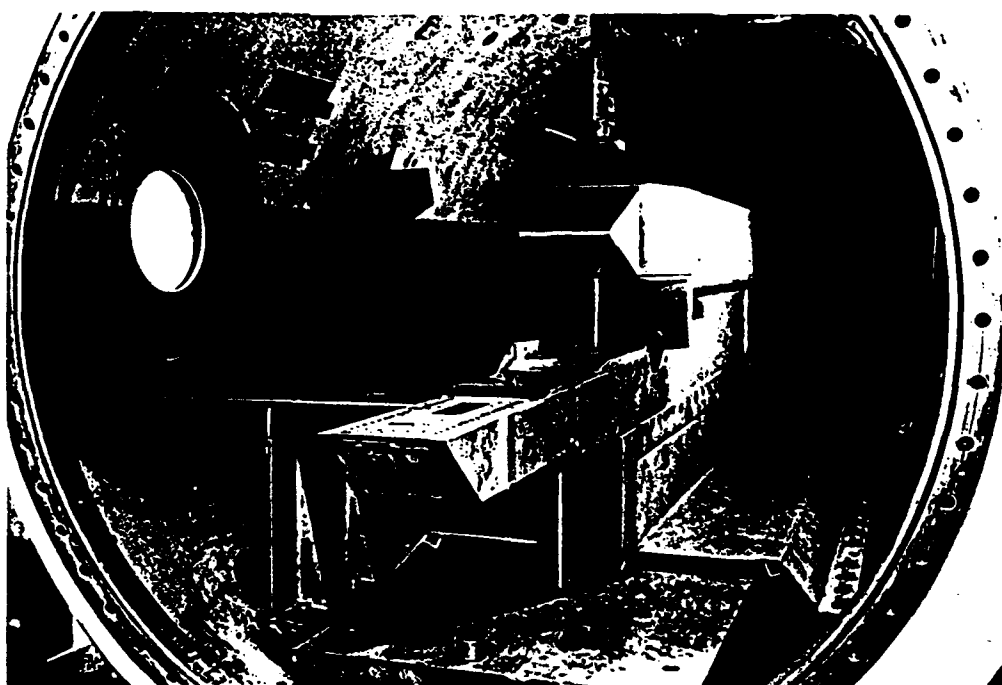


FIGURE 39 2D MODEL MOUNTED ON AERO-OPTICAL BENCH SYSTEM IN LENS FACILITY

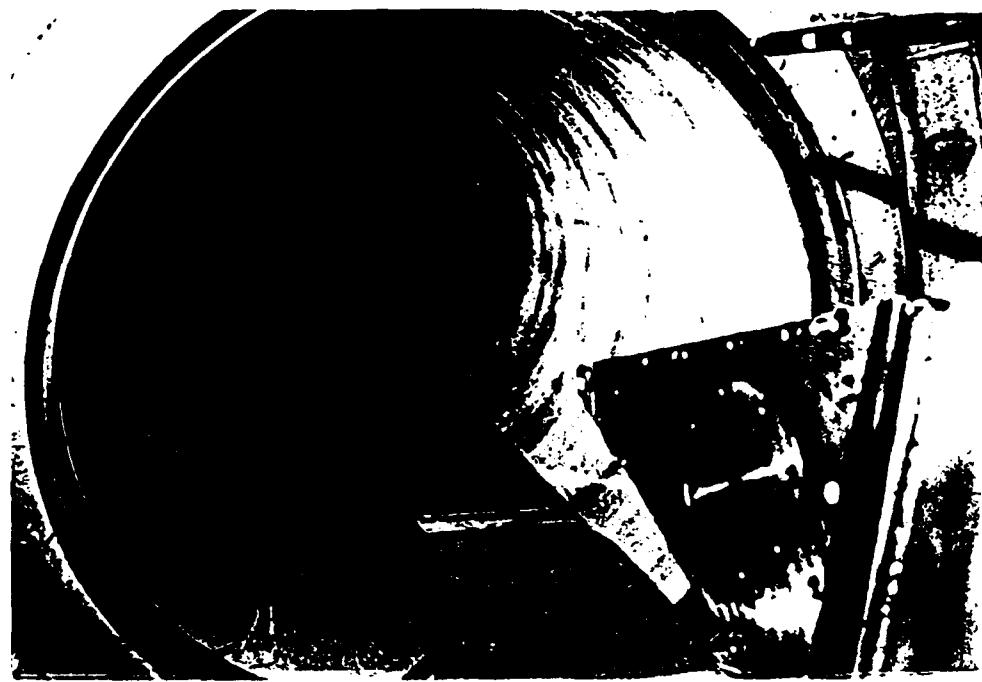


FIGURE 40 LASER DIAGNOSTICS THROUGH 2D CONFIGURATION

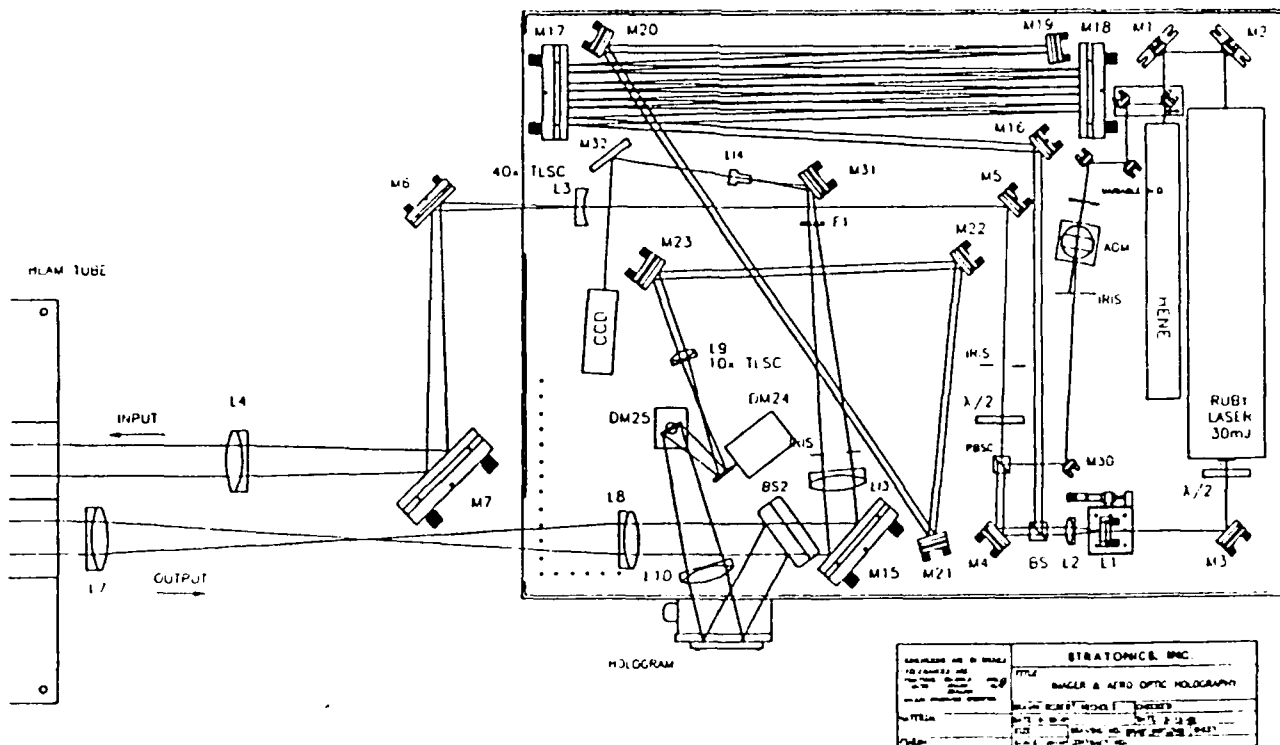


FIGURE 41 HOLOGRAPHY/IMAGER SYSTEM

STRATONICS, Inc

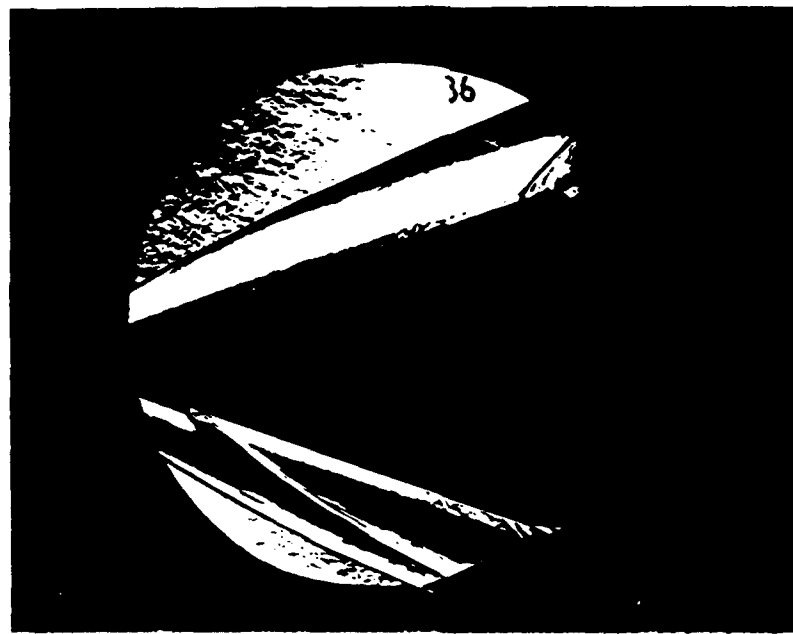


FIGURE 42 SCHLIEREN PHOTOGRAPHY OF FLOW OVER 2D CONFIGURATION WITHOUT COOLING OVER WINDOW ON LOWER SURFACE

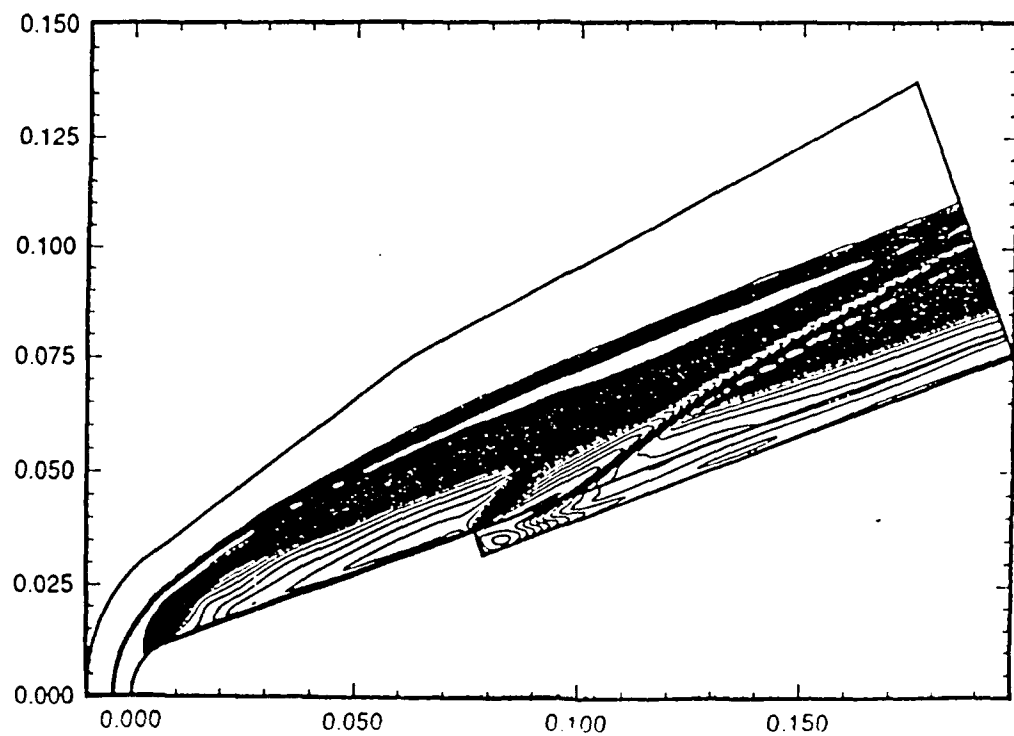


FIGURE 43 SCHLIEREN PHOTOGRAPHY OF FLOW OVER 2D CONFIGURATION WITHOUT 1.5 MATCHED PRESSURE COOLING OVER WINDOW ON LOWER SURFACE

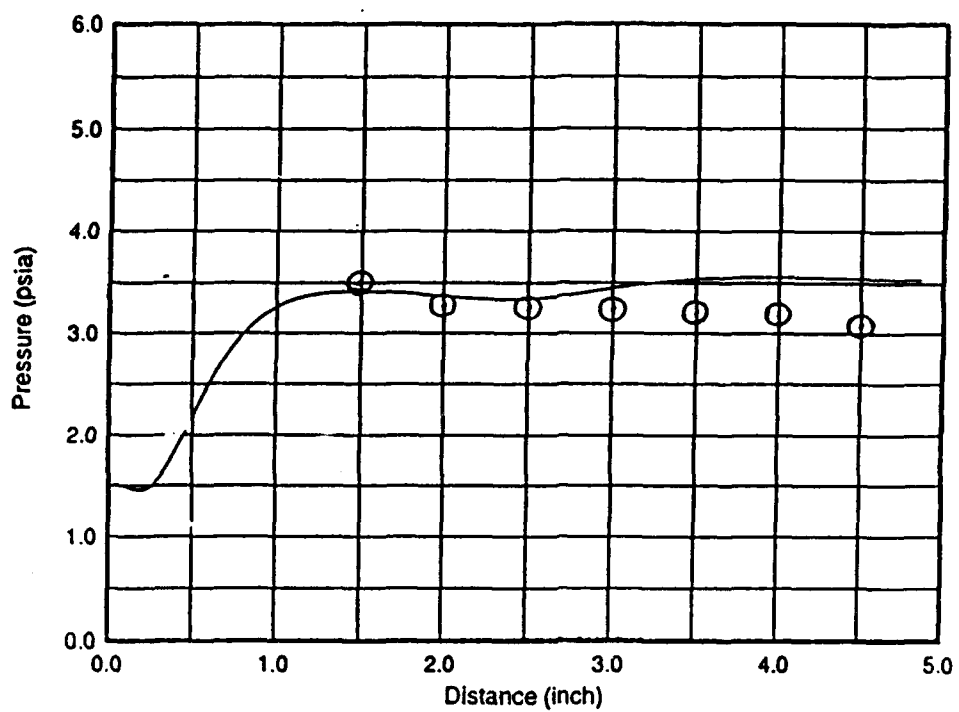


FIGURE 44 PRESSURE ALONG WINDOW SURFACE (CASE 301)

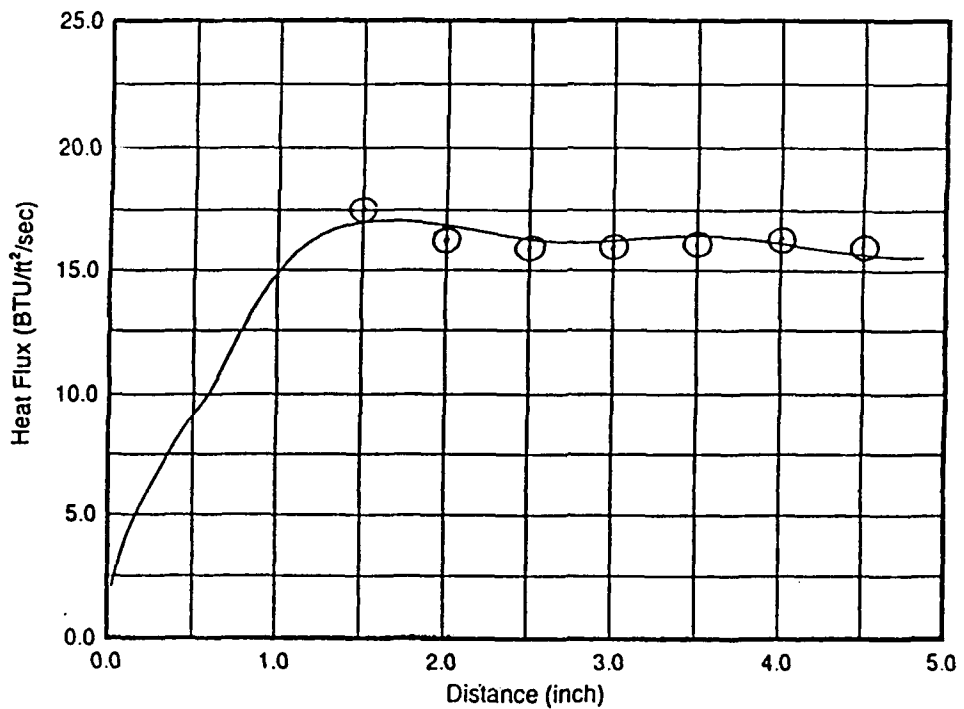


FIGURE 45 HEAT FLUX ALONG WINDOW SURFACE (CASE 301)



FIGURE 46 SCHLIEREN PHOTOGRAPHS

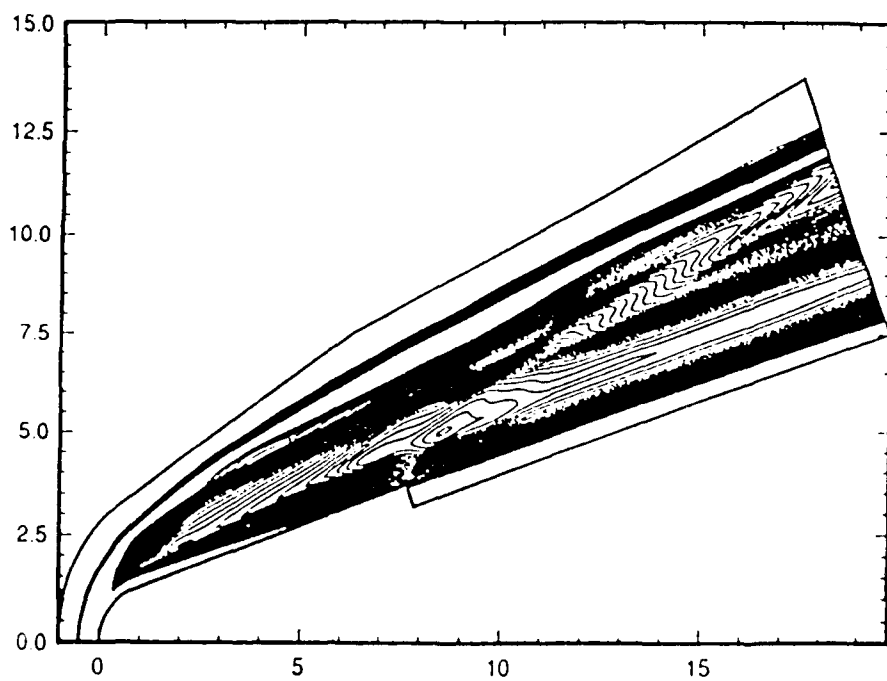


FIGURE 47 DENSITY CONTOUR (CASE 343, N_2 COOLANT)

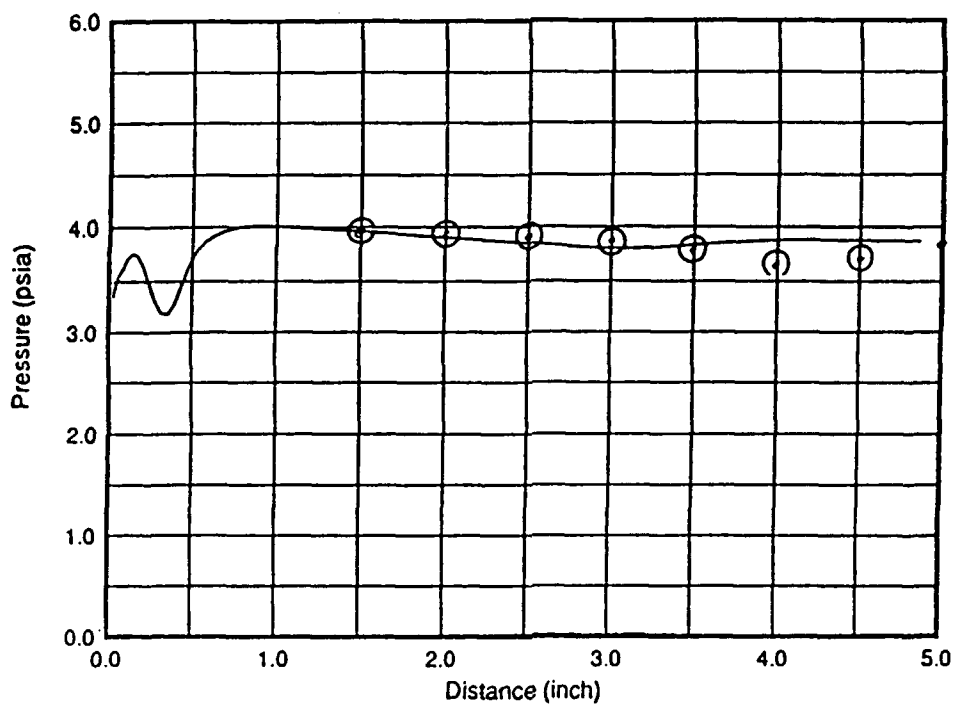


FIGURE 48 PRESSURE ALONG WINDOW SURFACE (CASE 343)

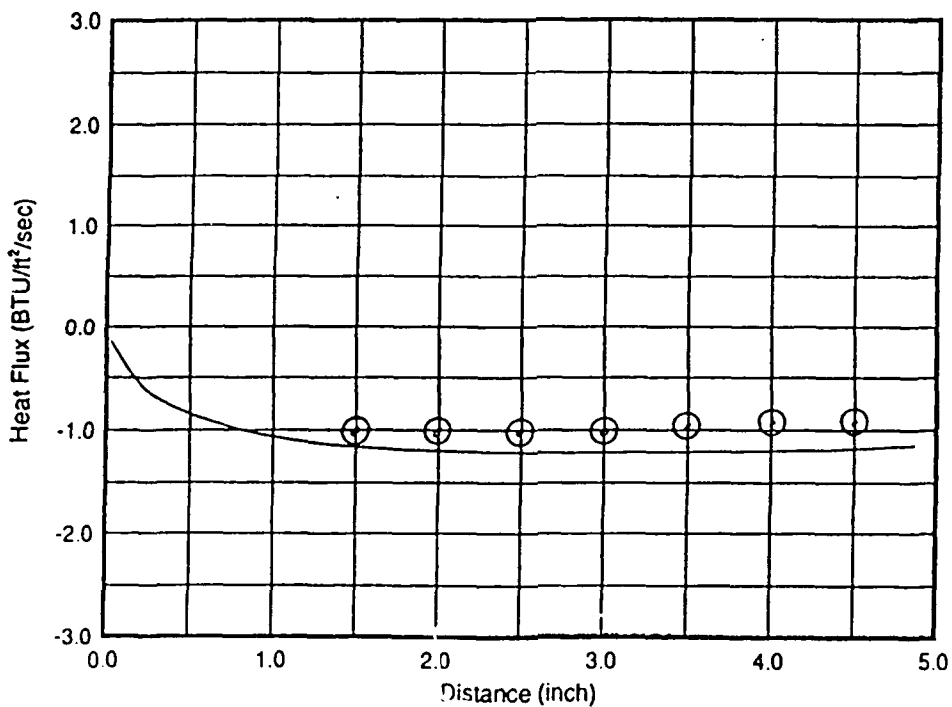


FIGURE 49 HEAT FLUX ALONG WINDOW SURFACE (CASE 343)

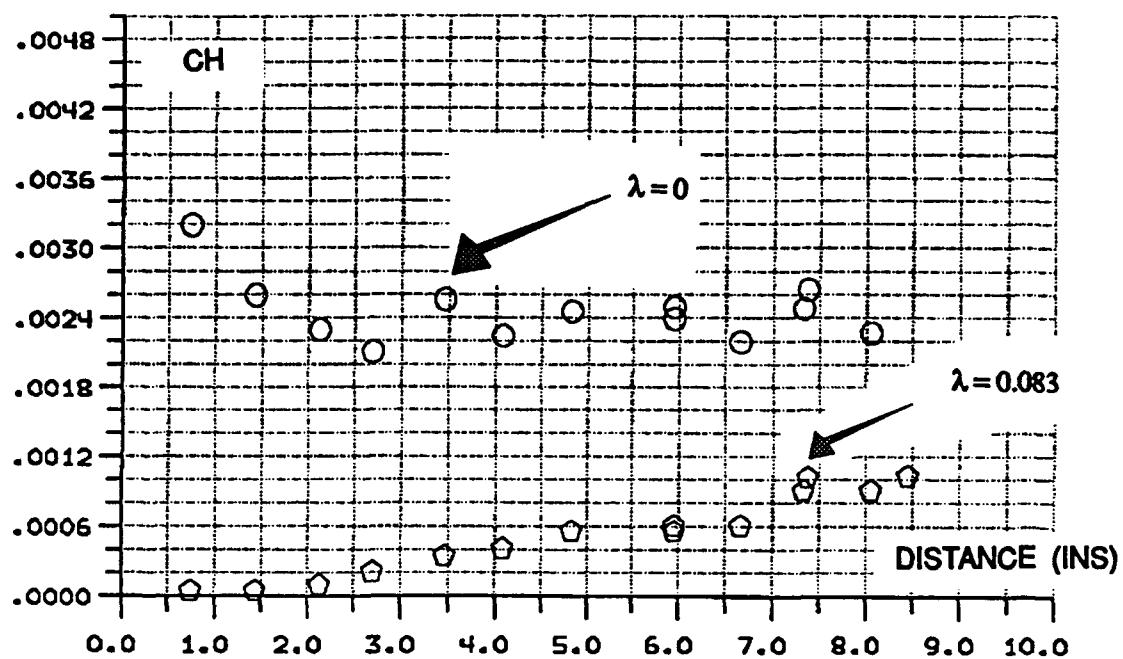


FIGURE 50 WINDOW COOLING MEASUREMENTS ON 2D CONFIGURATION FOR TEST POINT 3.

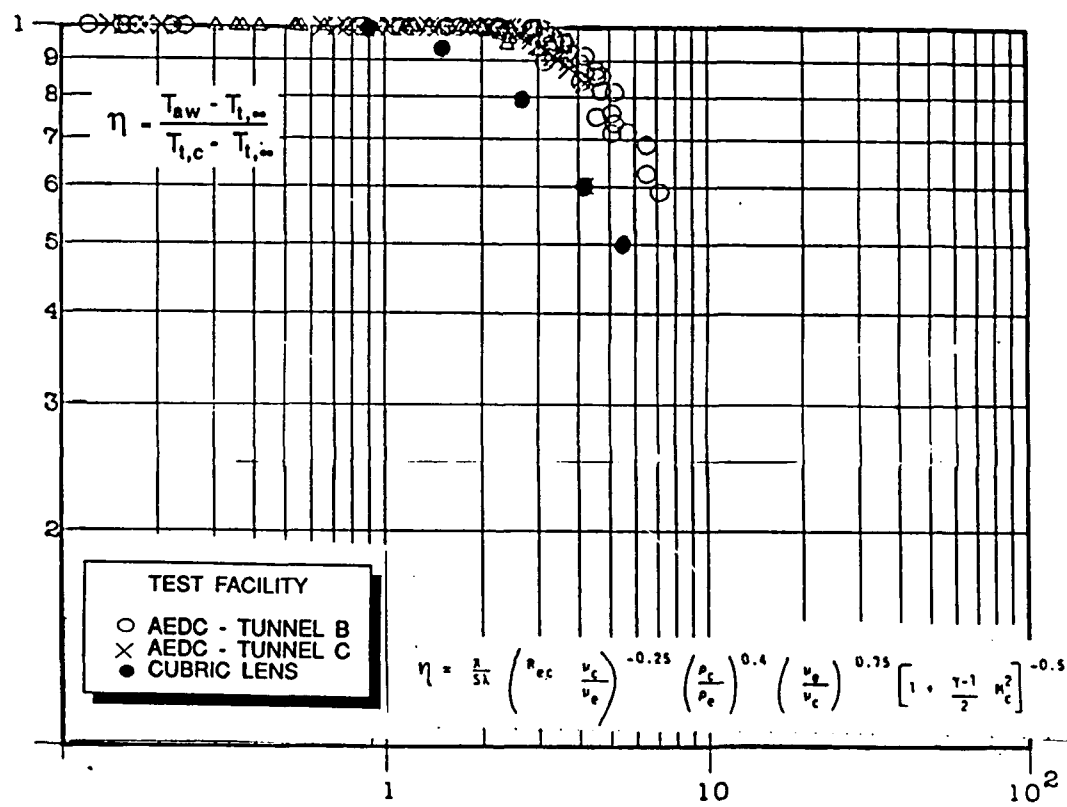


FIGURE 51 LENS HIGH VELOCITY MEASUREMENT COMPARED WITH HED CORRELATION OF EARLIER DATA.

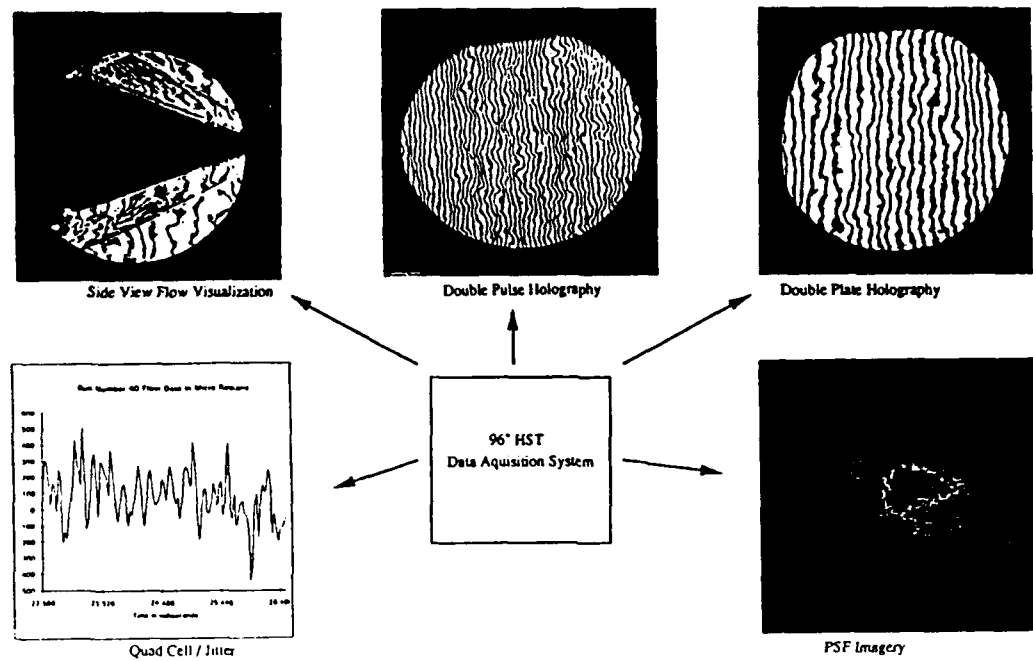


FIGURE 52 AERO-OPTIC RAW DATA EXAMPLES - N₂ 2X COOLANT

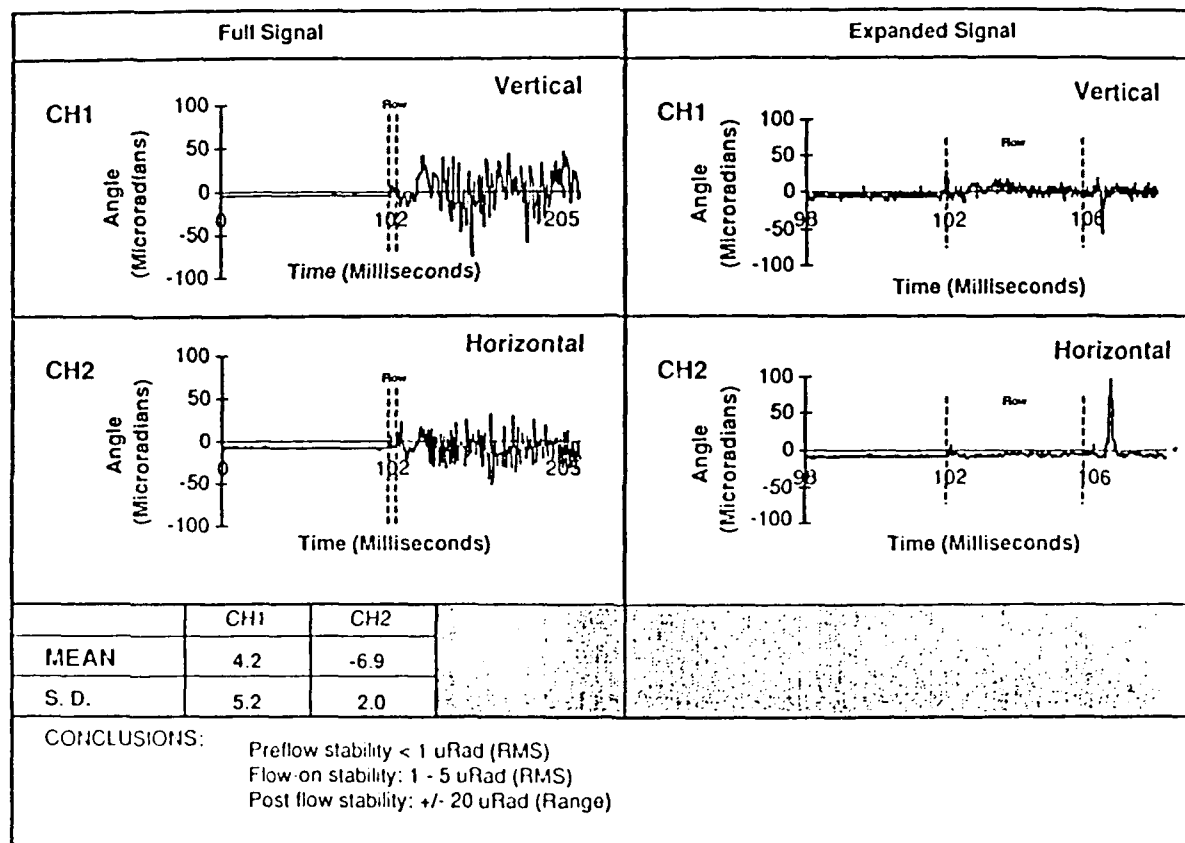
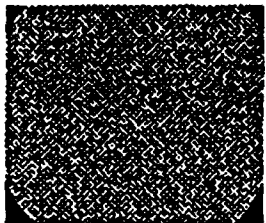
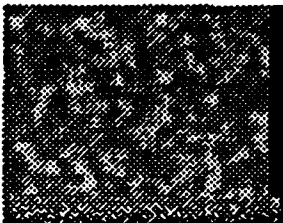


FIGURE 53 FLAT-PLATE MODEL (RUN 9) - PINHOLE MASK BSE SENSOR

- Validation of Fringe Analysis Software
- Allows quantitative study of how image quality is affected by:
 - RMS Wavefront error
 - Flowfield length scales

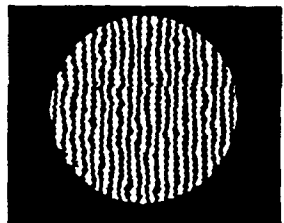


White.img
Computer Generated
"Whitenoise" Wavefront/
Phase Distribution



P2923-01.img
"Smoothed" Wavefront,
after 2-D convolution

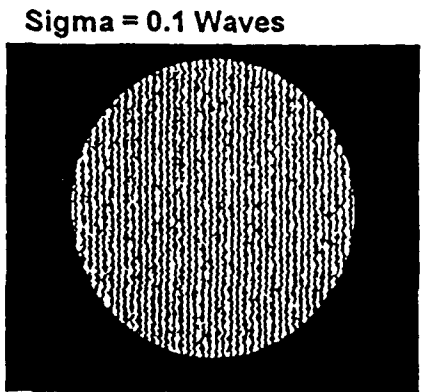
- Adjust Length Scales
by 2-D window size
- Adjust RMS P-V by overall
scale Parameter



RMS1.img
Fringe pattern ("Intensity
Distribution"). Can adjust:

- Fringe Count
- Fringe Orientation
- Aperture Size

FIGURE 54 SIMULATION OF FLOWFIELD ABERATED WAVEFRONTS

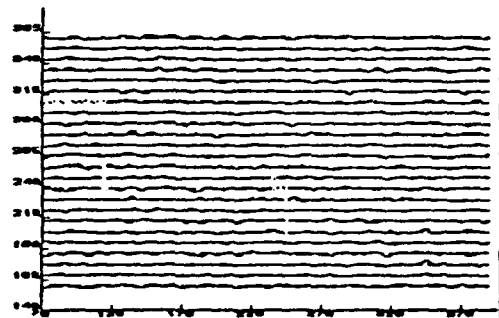


Sigma = 0.1 Waves

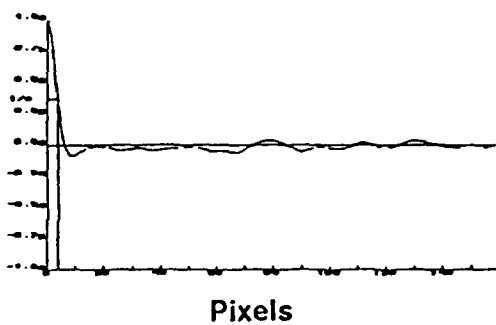
Fringe Tracking Analysis

- Digitize Interferogram
- Track Fringes
- Fit Plane Wave
- Measure RMS and Peak-to-Valley
- Measure Phase Correlation Function and Length Scale

Fringe Center Plot



Phase Correlation Function



Pixels

FIGURE 55 FRINGE TRACKING INTERFEROMETRY ANALYSIS

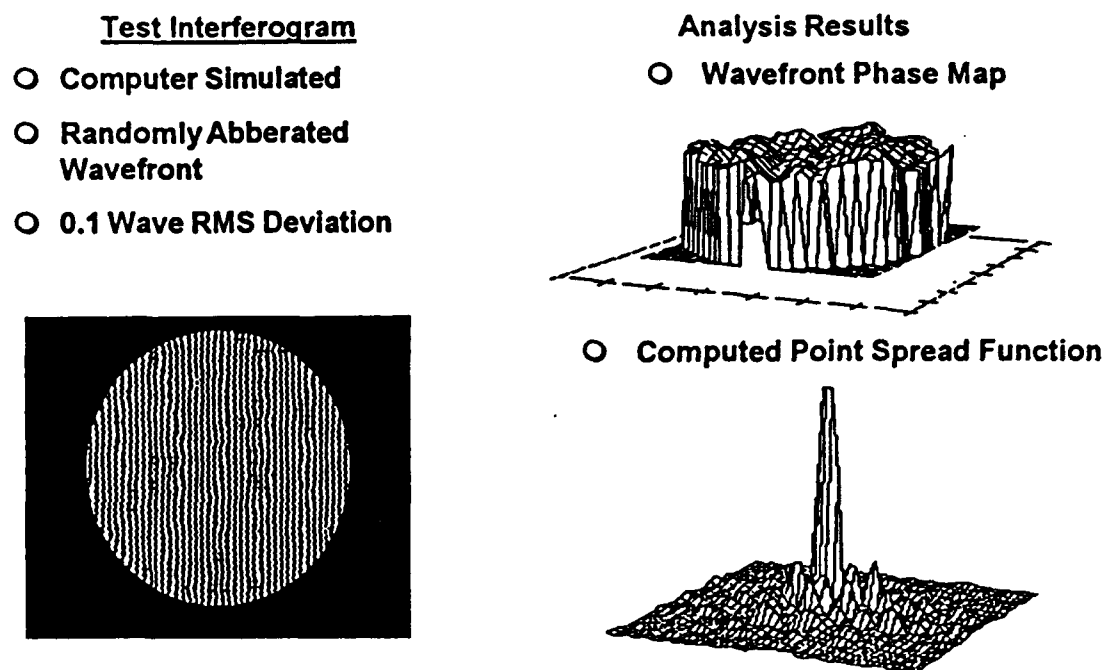


FIGURE 56 SPATIAL FOURIER TRANSFORM METHOD OF FRINGE ANALYSIS

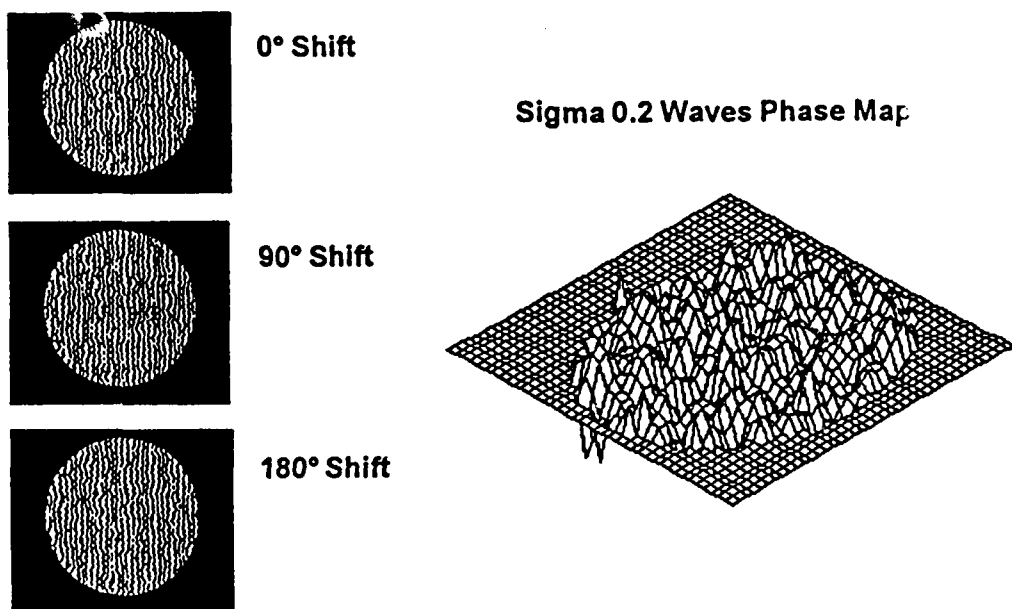


FIGURE 57 PHASE SHIFTING INTERFEROMETRY ANALYSIS

- o 96" Tunnel
- o Computed rms wavefront error = .36 waves

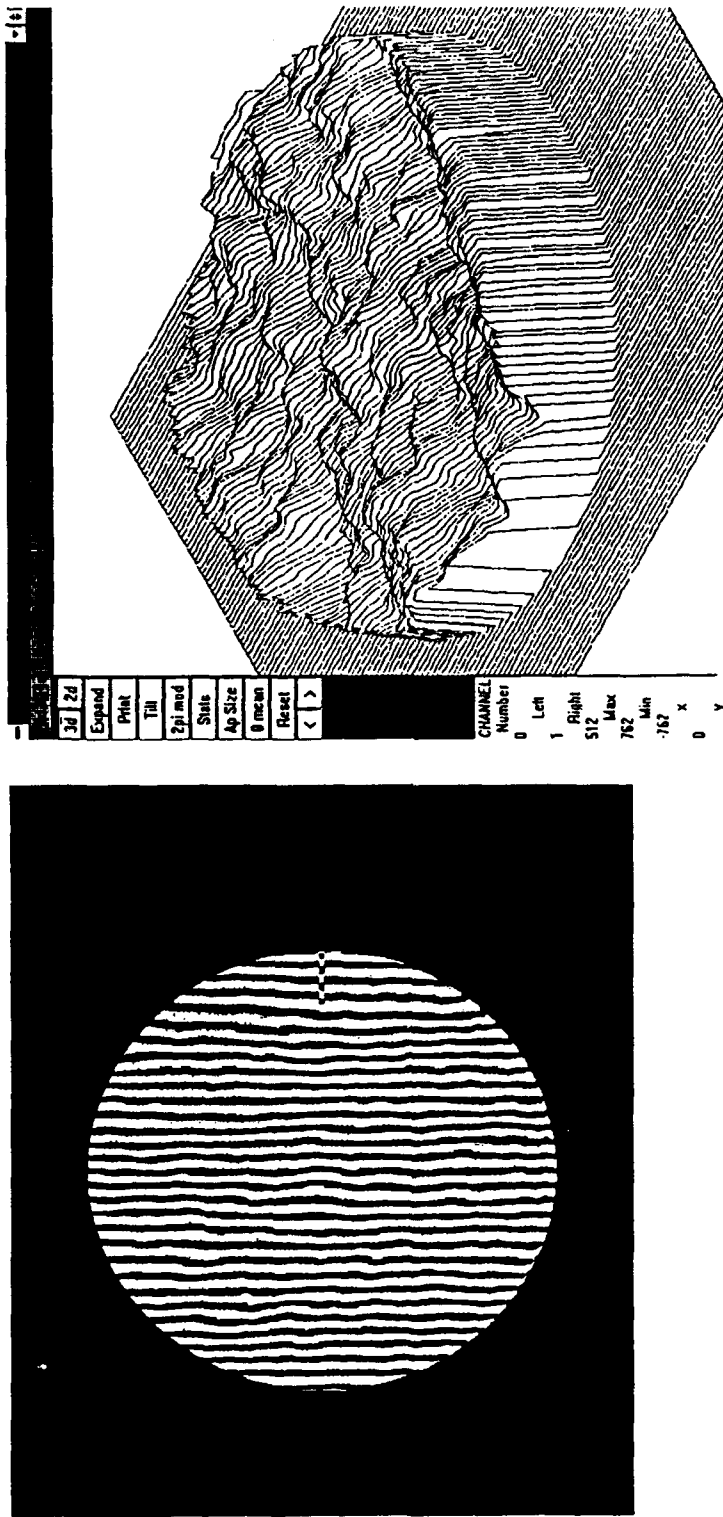
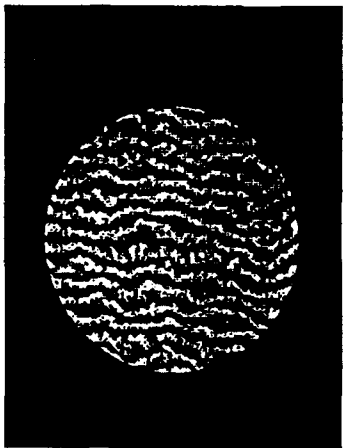


Figure 58 . Spatial Fourier Transform Analysis of Run 46.

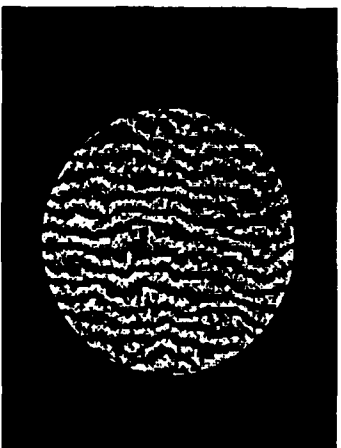
46sft.tif

- 96" Tunnel
- Computed rms waveform
- error = .38 waves

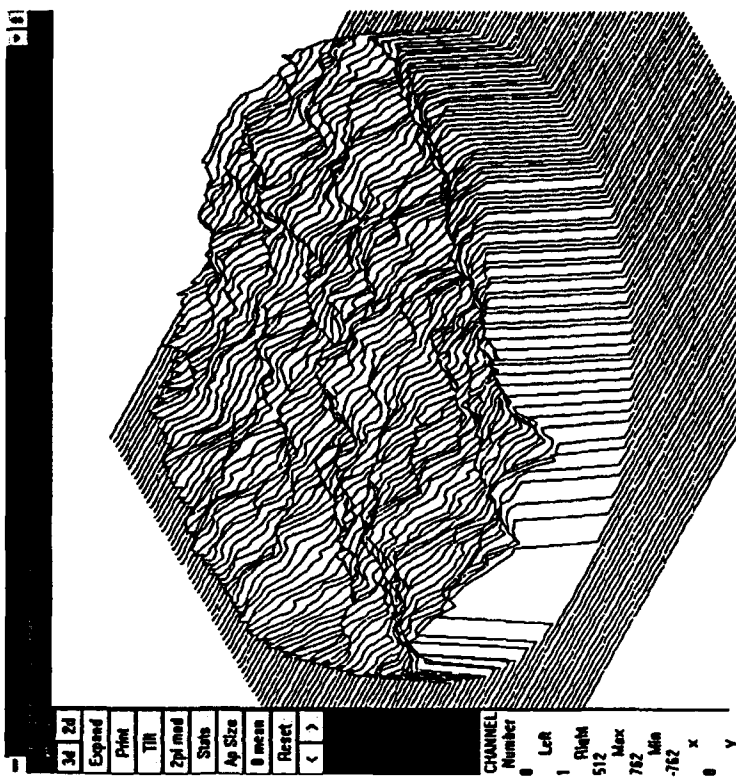
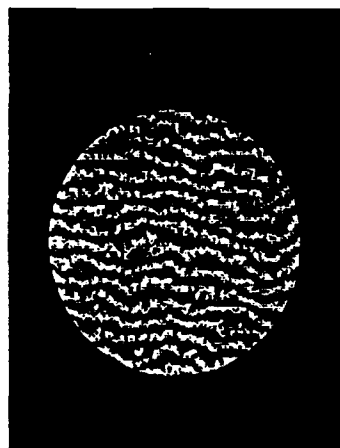
0 Degrees



90 Degrees



180 Degrees



Acquired Interferograms

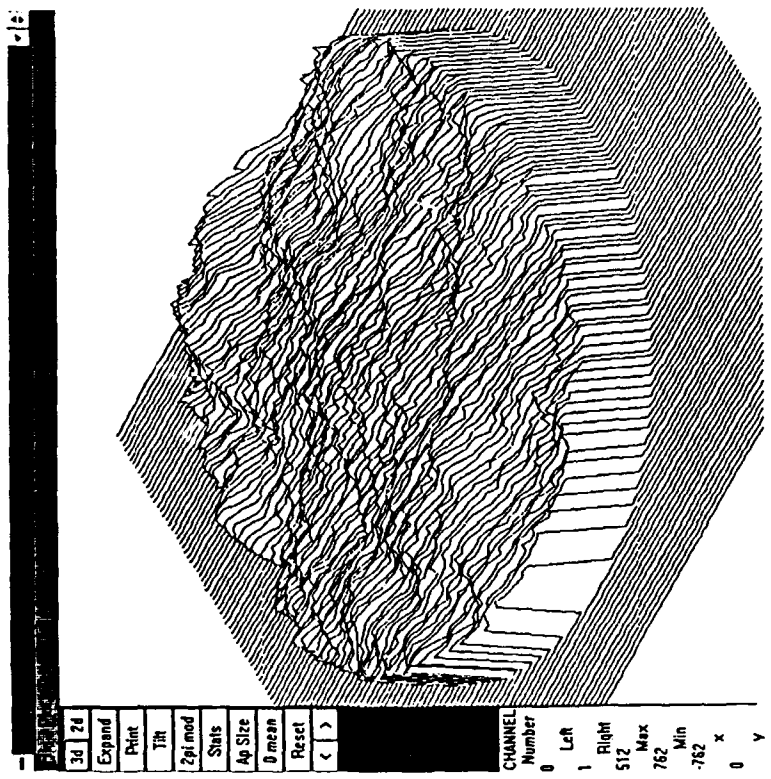
Reconstructed Phase

Figure 59 . Phase Shifting Analysis of Run 46.

46psi.tif

Comparison of helium and nitrogen coolents (Runs 47 and 46)

Helium, sigma = 0.31 waves



Nitrogen, Sigma = 0.38 waves

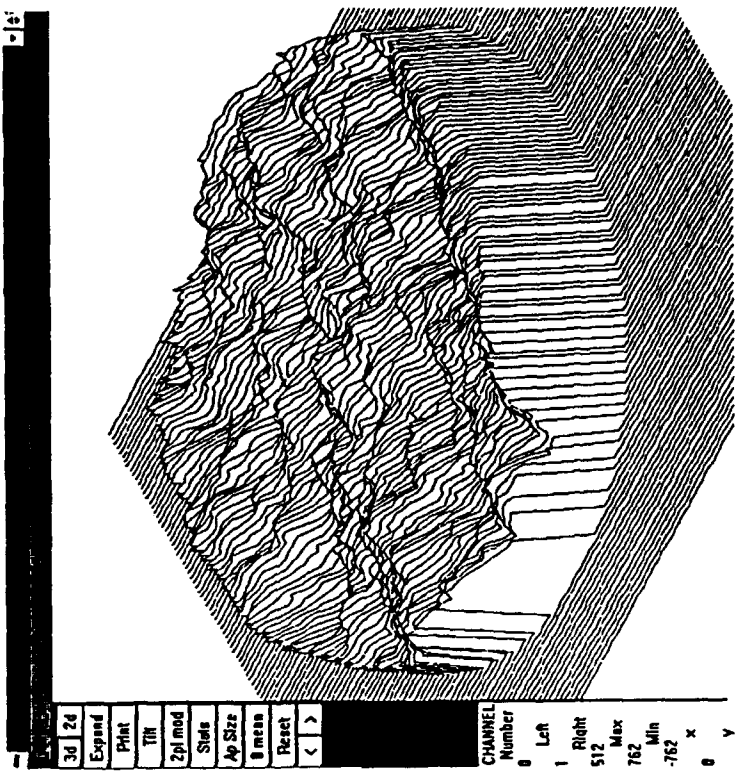


Figure 60 Phase Shifting Analysis

46psi.tif